

State Estimation of Marine Vessels Affected by Waves by Unmanned Aerial Vehicles^{*,**}

Filip Novák^{a,*}, Tomáš Báča^a, Ondřej Procházka^a and Martin Saska^a

^aDepartment of Cybernetics, Faculty of Electrical Engineering, Czech Technical University in Prague, Czech Republic

ARTICLE INFO

Keywords:

Mathematical model of marine vessel
State estimation
State prediction
Sensor fusion
Unmanned aerial vehicle
Unmanned surface vehicle

Abstract

A novel approach for robust state estimation of marine vessels in rough water is proposed in this paper to enable tight collaboration between Unmanned Aerial Vehicles (UAVs) and a marine vessel, such as cooperative landing or object manipulation, regardless of weather conditions. Our study of marine vessel (in our case Unmanned Surface Vehicle (USV)) dynamics influenced by strong wave motion has resulted in a novel nonlinear mathematical USV model with 6 degrees of freedom (DOFs), which is required for precise USV state estimation and motion prediction. The proposed state estimation approach fuses data from multiple sensors onboard the UAV and the USV to enable redundancy and robustness under varying weather conditions of real-world applications. The proposed approach provides estimated states of the USV with 6 DOFs and predicts its future states to enable tight control of both vehicles on a receding control horizon. The proposed approach was extensively tested in the realistic Gazebo simulator and successfully experimentally validated in many real-world experiments representing different application scenarios, including agile landing on an oscillating and moving USV. A comparative study indicates that the proposed approach significantly surpassed the current state-of-the-art.

1. INTRODUCTION

Tight collaboration between multirotor Unmanned Aerial Vehicles (UAVs) and Manned and Unmanned Surface Vehicles (USVs), i.e. ships or boats Fossen (2011) (Figure 1) is required in numerous offshore as well as freshwater applications. The USVs-UAVs team is beneficial in searching for and removing garbage from water Han and Ma (2021), providing assistance in the aftermath of disasters Murphy et al. (2006, 2008), transporting materials and objects from one place to another Steenken et al. (2001), cooperation with rescue services Ramirez et al. (2011), gathering environmental data and water quality monitoring Young et al. (2017).

An important aspect of any tight multi-robot collaboration is mutual localization among the teammates Walter et al. (2018a). Relative states between UAVs and USVs, which consist of position, orientation, velocity, and angular velocity, are required in most of complex multi-robot missions Oh et al. (2006). Using this information, the UAV can precisely follow the USV Gonzalez-Garcia et al. (2021), explore different parts of the environment Murphy et al. (2006), or land on the USV Djapic et al. (2015); Gupta et al. (2023); Li et al. (2023); Polvara et al. (2018); Xu et al. (2020a); Santos et al. (2024). The landing task was selected

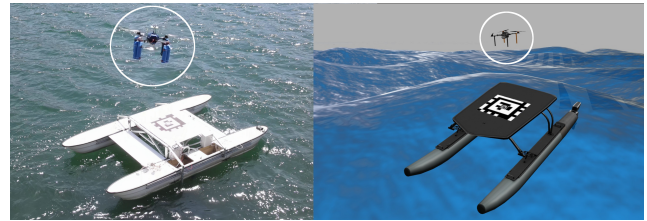


Figure 1: UAV used in the presented research cooperating together with a USV equipped with a landing platform.

as a key study of the approach presented in this paper due to its sensitivity to precise data. In order to land on the USV, the UAV requires accurate localization and state estimation of the landing platform placed onboard the USV Djapic et al. (2015) and motion prediction of the USV in case of the rough sea surface.

The ability of the UAV to land on the USV in all weather and sea conditions is required for battery recharging, as UAV flight time is greatly limited by battery capacity Aissi et al. (2020). Other examples include unloading cargo carried by the UAV Grlj et al. (2022) and transporting the UAV to the area of its operation Shao et al. (2019). The USV can also provide a safe docking spot for the UAV in the event of inclement weather Aissi et al. (2020). A safe landing, while avoiding critical situations leading to damage to the aerial vehicle as shown in Figure 2, requires designing a robust approach for estimating and predicting USV states with 6 Degrees of Freedom (DOFs) affected by wave motions and multi-sensor perception for various weather conditions, as presented in this paper.

* This work has been supported by the Technology Innovation Institute - Sole Proprietorship LLC, UAE, under the Research Project Contract No. TII/ARRC/2055/2021, CTU grant no SGS23/177/OHK3/3T/13 and the Czech Science Foundation (GAČR) under research project No. 23-06162M.

**Multimedia materials: <https://mrs.fel.cvut.cz/papers/usv-state-estimation>

*Corresponding author

✉ filip.novak@fel.cvut.cz (F. Novák)

🌐 <https://mrs.fel.cvut.cz/filip-novak> (F. Novák)

ORCID(s): 0000-0003-3826-5904 (F. Novák); 0000-0001-9649-8277 (T.

Báča); 0009-0009-2224-750X (O. Procházka); 0000-0001-7106-3816 (M. Saska)

2. RELATED WORKS

The approaches to state estimation can be separated into two groups. The first group consists of systems relying on Global Navigation Satellite System (GNSS) (e.g., Global Positioning System (GPS)) and Inertial Measurement Unit (IMU) to estimate the states Assaf et al. (2018); Ccolque-Churquipa et al. (2018); Deep et al. (2018); Kwak and Sung (2018). To obtain the USV states relative to the UAV states, the estimated states of the USV must be sent to the UAV via a reliable communication link with sufficient rate and bandwidth. However, the required communication link is challenging to achieve in real-world deployment Tran and Ahn (2019). Moreover, the precision of GNSS Drawil et al. (2013) is not sufficient in order of magnitude for landing UAV into a recharging box, which is often required.

State estimation methods in the second group use vision-based relative localization systems to provide information about desired targets Krogius et al. (2019); Olson (2011); Walter et al. (2018a,b); Wang and Olson (2016); Xiao et al. (2017). The concept of these systems enables them to be put onboard UAVs that use them to estimate USV states without the need for any communication link. However, such systems of relative localization require a target in a detectable position. Usually, the system must be close to the target, and the vision sensor, e.g., the camera, must see the target in its frame to provide measurements. Further, the performance and reliability of these systems depend on weather and lighting conditions Krogius et al. (2019); Olson (2011); Wang and Olson (2016), and the estimation of target tilt using only camera images is inaccurate Olson (2011); Walter et al. (2018a,b); Xiao et al. (2017).

In all approaches discussed above, the gained sensor data need to be processed in real-time to estimate the desired states for fast control loop. Most of the approaches address state estimation using the Kalman filter Fossen and Perez (2009); Julier and Uhlmann (1997); Kalman (1960); Liu et al. (2019); Malyuta et al. (2020); Naab and Zheng (2022). The Kalman filter fuses measurements from different sensors to obtain accurate state estimation of a given system Haykin (2001); Ribeiro (2004), and further requires a mathematical model of such a system to estimate its states. The full 6 DOF nonlinear mathematical models of USV are presented in Fossen (1994, 2002, 2011). These works also present linearization of the nonlinear USV model and discuss the methods for wave motion filtering. However, the estimation of the USV states with 6 DOFs in waves is not presented. The approach Fossen and Perez (2009) uses a simplified 3 DOF linear model based on Fossen (1994, 2002, 2011) for positioning and heading control. The 3 DOF mathematical USV models consisting of planar position and heading are also considered in Tomera (2012); Wang et al. (2021a); Wirtensohn et al. (2016); Xu et al. (2020b). As discussed later, the 3 DOF state estimation is not sufficient in harsh conditions as the heave motion and roll and pitch angles are not observable by these approaches.

From the available literature we selected the most relevant papers to the presented approach. Table 1 summarizes

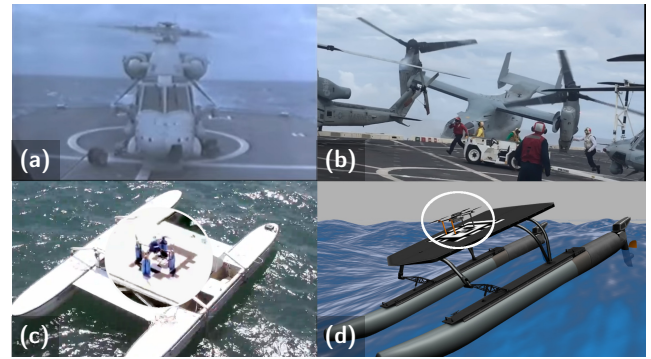


Figure 2: Unsuccessful landing on a marine vessel without the landing pad motion detection and prediction (mainly the heave motion was difficult to observe), shown in (a) and (b), serves as motivation to create a robust USV state estimation system in 6 DOFs to ensure safe autonomous landing in rough water and different real-world conditions as shown in snapshots from our system deployment (c) and (d).

the comparison of these state-of-the-art works with the approach proposed in this paper. Most of the works use simplified USV state vectors representing models with 3 DOFs (planar translation and heading) Fossen and Perez (2009); Tomera (2012); Wang et al. (2021b); Wirtensohn et al. (2016); Xu et al. (2020b). The system presented in Abujoub et al. (2018) estimates the USV with 5 DOFs. The approach in Polvara et al. (2018) is the only one we found that estimates the USV with 6 DOFs. However, the wave motion is not considered in Polvara et al. (2018), which may cause critical failures (see Figure 2 (a) and (b)) and restricts using this work in real-world conditions or to very large marine vessels not-influenced by waves. In the available literature, the wave dynamics in USV model during estimation of the USV states is considered only with lower DOFs Fossen and Perez (2009); Tomera (2012); Wirtensohn et al. (2016), which simplifies the problem and may lead to failures due to unobservable oscillation and heave motion (see Figure 2). Our work overperforms the available literature by considering the most complex situation with a state vector with a full 6 DOFs, where wave motion is taken into account for all USV states.

Regarding the ability to predict future USV states, the approach in Abujoub et al. (2018) is able to compute such a prediction to exhibit periodic behavior resembling wave motions. However, only 2 DOFs (roll and pitch angles) are predicted, which is insufficient for tight cooperation and landing. The approach Abujoub et al. (2018) assumes observing waves in filtered raw sensor data as periodic motion. Then the main components of these periodic signals are identified using the Fast Fourier Transform and used to predict future roll and pitch angles. Data are obtained from 3 simulated single pulse Light Detection and Ranging (LiDAR) devices assuming that laser beam from each LiDAR device hits the desired area on the landing board, which can be very problematic in a real-world deployment. The work Abujoub

Work	Designed for UAVs	Number of DOFs	Wave dynamics in USV model	Predict future states including wave motions	Ability to fuse sensor data from UAV and USV	Real-world deployment
Wang et al. (2021b)	No	3	No	No	No	No
Tomera (2012)	No	3	Yes	No	No	Yes
Fossen and Perez (2009)	No	3	Yes	No	No	No
Wirtensohn et al. (2016)	No	3	Yes	No	No	Yes
Xu et al. (2020b)	Yes	3	No	No	No	Yes
Abujoub et al. (2018)	Yes	5	No	Yes	No	No
Polvara et al. (2018)	Yes	6	No	No	No	No
This work	Yes	6	Yes	Yes	Yes	Yes

Table 1

A comparison of the available USV state estimation approaches related to this work.

et al. (2018) was not verified in real-world conditions, and the considered assumptions on sensors uncertainty are not realistic based on our experimental analyses. The works Tomera (2012); Wirtensohn et al. (2016); Xu et al. (2020b) deployed in the real world use only a USV state vector with 3 DOFs and do not predict future USV states.

2.1. Contributions

A novel solution for the required 6 DOF state estimation and prediction of a moving USV on a rough water surface by a UAV is proposed in this paper. The main contributions of the presented method going beyond the relevant literature summarized above are the following:

- novel nonlinear 6 DOF USV mathematical model containing wave dynamics,
- derivation of a linear model from our novel nonlinear 6 DOF USV mathematical model,
- prediction of future USV states with 6 DOFs,
- a robust method for the state estimation of a moving USV with 6 DOFs on a rough water surface using presented mathematical models.

All these contributions were verified in numerous simulations and real-world experiments. The overall performance was compared with state-of-the-art methods.

2.2. Problem statement

This paper tackles the problem of accurate USV state estimation with 6 DOFs by a UAV on a rough water surface and prediction of the future USV states. This enables planning the UAV trajectories to be optimal and efficient for reliable coordination with USV and landing onboard USV in harsh conditions being our target scenarios. One of the addressed sub-problems is creating a 6 DOF mathematical model of the USV moving on a rough water surface, which is used for estimation and prediction. The proposed estimation approach is designed for a real-world environment, where limits of individual global and onboard sensors are considered to ensure the robustness of the entire solution in real-world conditions.

It is assumed that the UAV is equipped by GNSS receiver, flight controller with IMU, and down-looking cameras to utilize global and onboard localization systems, whose measurements are processed by the onboard CPU. The USV carries GNSS receiver, IMU, and pattern detectable from UAV onboard sensors. Moreover, a communication link between the UAV and the USV is required for transferring onboard sensor data from the USV to the UAV, at least on 1 Hz. However, the designed system is able to work in the event of an unavailable communication link by using just the UAV onboard sensors. It is further assumed that the USV is moving at a speed where the UAV is able to follow it – based on our experimental evaluation, we require the USV speed to be less than 90% of the maximal UAV speed.

3. MATHEMATICAL USV MODEL

The full nonlinear USV model is used to fuse the data of multiple sensors and additionally predict the future states of the USV. The proposed approach in this paper focuses on state estimation and prediction of the USV moving on wavy water surfaces with a particular interest in parameters required for precise landing in rough conditions. Therefore, the regularly used USV model needs to be extended by wave dynamics to obtain sufficient estimation and prediction accuracy (Section 4).

The USV is modeled as a rigid body with 6 DOFs of translation and rotation in 3D (see Figure 3). The longitudinal motion of the USV in direction of the x_b axis is called *surge*. The rotation around the x_b axis is known as *roll*. *Sway* is lateral motion, or sideways motion, in the direction of the y_b axis. The rotation corresponding to the y_b axis is *pitch*. The last motion, known as *heave*, takes place in a vertical direction with respect to the z_b axis, and *yaw* is the corresponding rotation. Table 2 summarizes notation of USV motion variables corresponding to the presented DOFs: position and orientation, their derivatives representing linear and angular velocities, and forces and torques.

DOF	meaning	Positions and Euler angles	Linear and angular velocities	Forces and torques
1	surge	x	u	τ_x
2	sway	y	v	τ_y
3	heave	z	w	τ_z
4	roll	ϕ	p	τ_ϕ
5	pitch	θ	q	τ_θ
6	yaw	ψ	r	τ_ψ

Table 2

The notation of USV motion variables.

3.1. Kinematics

First, we define the kinematic transformation to describe the motion of the USV in different coordinate frames. During analysis of the USV motion, two coordinate frames are defined as shown in Figure 4. The first one is a body-fixed frame of the USV that is put into the center of gravity of the USV. The second one is a global coordinate frame whose origin is fixed to the Earth's surface. It is assumed that the position and orientation of the USV are expressed in a global coordinate frame, while linear and angular velocities are described in a body-fixed coordinate frame. According to the coordinate frames presented above, the following vectors describe the USV motion

$$\boldsymbol{\eta} = (\mathbf{p}^T, \boldsymbol{\Theta}^T)^T = (x, y, z, \phi, \theta, \psi)^T, \quad (1)$$

$$\mathbf{v} = (\mathbf{v}^T, \boldsymbol{\omega}^T)^T = (u, v, w, p, q, r)^T, \quad (2)$$

$$\boldsymbol{\tau} = (\boldsymbol{\tau}_p^T, \boldsymbol{\tau}_\Theta^T)^T = (\tau_x, \tau_y, \tau_z, \tau_\phi, \tau_\theta, \tau_\psi)^T, \quad (3)$$

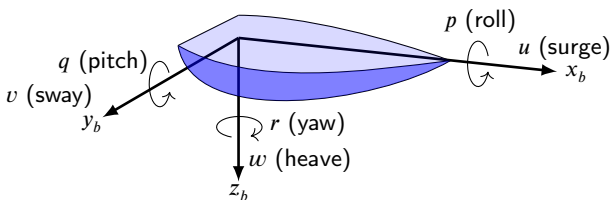
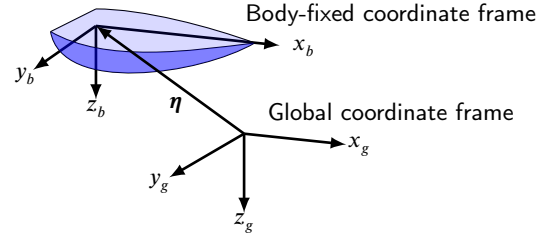
where $\boldsymbol{\eta}$ denotes position $\mathbf{p} = (x, y, z)^T$ and orientation $\boldsymbol{\Theta} = (\phi, \theta, \psi)^T$ in terms of intrinsic Euler angles Diebel (2006) in a global coordinate frame. The vector \mathbf{v} denotes linear velocity $\mathbf{v} = (u, v, w)^T$ and angular velocity $\boldsymbol{\omega} = (p, q, r)^T$ in a body-fixed coordinate frame. The term $\boldsymbol{\tau}$ represents forces $\boldsymbol{\tau}_p = (\tau_x, \tau_y, \tau_z)^T$ and torques $\boldsymbol{\tau}_\Theta = (\tau_\phi, \tau_\theta, \tau_\psi)^T$ relative to the body-fixed coordinate frame.

The transformation of body-fixed frame variables to global variables is given by

$$\dot{\mathbf{p}} = \mathbf{J}_1(\boldsymbol{\Theta})\mathbf{v}, \quad (4)$$

$$\dot{\boldsymbol{\Theta}} = \mathbf{J}_2(\boldsymbol{\Theta})\boldsymbol{\omega}, \quad (5)$$

where $\mathbf{J}_1(\boldsymbol{\Theta})$ and $\mathbf{J}_2(\boldsymbol{\Theta})$ are functions of the current Euler angles $\boldsymbol{\Theta}$. The $\dot{\mathbf{p}}$ denotes the velocity of the USV in the global frame, while $\dot{\boldsymbol{\Theta}}$ denotes the angular rates of Euler angles.


Figure 3: Motion of the USV with 6 DOFs.

Figure 4: Two coordinate frames used for analyzing the USV motion.

The transformation $\mathbf{J}_1(\boldsymbol{\Theta})$ defines rotation from a body-fixed frame to global frame as

$$\mathbf{J}_1(\boldsymbol{\Theta}) = \mathbf{R}_\psi \mathbf{R}_\theta \mathbf{R}_\phi, \quad (6)$$

where \mathbf{R}_ψ is rotation around z-axis, \mathbf{R}_θ is rotation around y-axis, and \mathbf{R}_ϕ is rotation around x-axis. According to Fossen (2011), the transformation $\mathbf{J}_2(\boldsymbol{\Theta})$ is

$$\mathbf{J}_2(\boldsymbol{\Theta}) = \begin{pmatrix} 1 & \sin \phi \tan \theta & \cos \phi \tan \theta \\ 0 & \cos \phi & -\sin \phi \\ 0 & \frac{\sin \phi}{\cos \theta} & \frac{\cos \phi}{\cos \theta} \end{pmatrix}. \quad (7)$$

However, the transformation matrix $\mathbf{J}_2(\boldsymbol{\Theta})$ is not defined for $\theta = \frac{\pi}{2} + k\pi$, $k \in \mathbb{Z}$. A USV moving over water will likely not experience such a situation, but nevertheless, the solution to such a problem is to use two conventions of the Euler angles representations with different singularities. If the USV is close to the singularity point in one convention, it is switched to another convention.

Finally, the kinematic transformation is mathematically described as

$$\begin{pmatrix} \dot{\mathbf{p}} \\ \dot{\boldsymbol{\Theta}} \end{pmatrix} = \begin{pmatrix} \mathbf{J}_1(\boldsymbol{\Theta}) & \mathbf{O}_{3 \times 3} \\ \mathbf{O}_{3 \times 3} & \mathbf{J}_2(\boldsymbol{\Theta}) \end{pmatrix} \begin{pmatrix} \mathbf{v} \\ \boldsymbol{\omega} \end{pmatrix}, \quad (8)$$

or, equivalently,

$$\dot{\boldsymbol{\eta}} = \mathbf{J}(\boldsymbol{\eta})\mathbf{v}. \quad (9)$$

3.2. Nonlinear USV model

The novel nonlinear 6 DOF USV model is based on the marine vessel dynamics analysis presented in Fossen (1994, 2002, 2011). We adopted the equations and made assumptions detailed below to create a mathematical USV model suitable for state estimation tasks. Moreover, we introduce a novel mathematical model capturing wave dynamics and incorporate it into the USV model (Section 4). This results in the novel nonlinear 6 DOF USV model describing USV motion on a rough water surface presented in equations (58)–(65) in Section 4.

We introduce the basic nonlinear 6 DOF USV model as

$$\dot{\boldsymbol{\eta}} = \mathbf{J}(\boldsymbol{\eta})\mathbf{v}, \quad (10)$$

$$\dot{\mathbf{v}} = \mathbf{M}^{-1}(\boldsymbol{\tau} - \mathbf{C}(\mathbf{v})\mathbf{v} - \mathbf{D}(\mathbf{v})\mathbf{v} - \mathbf{g}(\boldsymbol{\eta})), \quad (11)$$

where

- $\mathbf{M} \in \mathbb{R}^{6 \times 6}$ represents the inertia matrix,
- $\mathbf{C}(\mathbf{v}) \in \mathbb{R}^{6 \times 6}$ denotes the matrix of Coriolis and centripetal terms,
- $\mathbf{D}(\mathbf{v}) \in \mathbb{R}^{6 \times 6}$ is the damping matrix,
- $\mathbf{g}(\boldsymbol{\eta}) \in \mathbb{R}^6$ represents gravitational force and torques,
- $\boldsymbol{\tau} \in \mathbb{R}^6$ denotes the vector forces acting on the USV, e.g., wave forces, wind forces, and control inputs.

The inertia \mathbf{M} is composed of two matrices

$$\mathbf{M} = \mathbf{M}_{RB} + \mathbf{M}_A. \quad (12)$$

The matrix \mathbf{M}_{RB} is the positive definite rigid-body mass matrix

$$\mathbf{M}_{RB} = \begin{pmatrix} m\mathbf{I}_{3 \times 3} & \mathbf{O}_{3 \times 3} \\ \mathbf{O}_{3 \times 3} & \mathbf{I}_b \end{pmatrix}, \quad (13)$$

where m is the mass of the USV and $\mathbf{I}_{3 \times 3}$ is the identity matrix. The \mathbf{I}_b is the inertia matrix, whose components I_x, I_y, I_z are the moments of inertia about the corresponding body-fixed frame axes x_b, y_b, z_b and $I_{xy} = I_{yx}, I_{xz} = I_{zx}, I_{yz} = I_{zy}$. The matrix \mathbf{M}_A is the virtual hydrodynamic added mass caused by a moving object in a fluid. The matrix \mathbf{M}_A is expressed as

$$\mathbf{M}_A = \begin{pmatrix} X_{\ddot{u}} & X_{\ddot{v}} & X_{\ddot{w}} & X_{\ddot{p}} & X_{\ddot{q}} & X_{\ddot{r}} \\ Y_{\ddot{u}} & Y_{\ddot{v}} & Y_{\ddot{w}} & Y_{\ddot{p}} & Y_{\ddot{q}} & Y_{\ddot{r}} \\ Z_{\ddot{u}} & Z_{\ddot{v}} & Z_{\ddot{w}} & Z_{\ddot{p}} & Z_{\ddot{q}} & Z_{\ddot{r}} \\ K_{\ddot{u}} & K_{\ddot{v}} & K_{\ddot{w}} & K_{\ddot{p}} & K_{\ddot{q}} & K_{\ddot{r}} \\ M_{\ddot{u}} & M_{\ddot{v}} & M_{\ddot{w}} & M_{\ddot{p}} & M_{\ddot{q}} & M_{\ddot{r}} \\ N_{\ddot{u}} & N_{\ddot{v}} & N_{\ddot{w}} & N_{\ddot{p}} & N_{\ddot{q}} & N_{\ddot{r}} \end{pmatrix}, \quad (14)$$

where elements $X_{\ddot{u}}, X_{\ddot{v}}, \dots, N_{\ddot{r}}$ are coefficients of hydrodynamic added mass.

The Coriolis and centripetal matrix $\mathbf{C}(\mathbf{v})$ is similar to the inertia matrix \mathbf{M} (12) composed of two matrices

$$\mathbf{C}(\mathbf{v}) = \mathbf{C}_{RB}(\mathbf{v}) + \mathbf{C}_A(\mathbf{v}). \quad (15)$$

The Coriolis and the centripetal term is a result of the rotation of the body-fixed reference frame. The \mathbf{C}_{RB} stands for rigid-body Coriolis and centripetal matrix. In order to move the rigid body in a fluid, the hydrodynamic Coriolis and centripetal matrix $\mathbf{C}_A(\mathbf{v})$ is defined as

$$\mathbf{C}_A(\mathbf{v}) = \begin{pmatrix} 0 & 0 & 0 & 0 & -C_3 & C_2 \\ 0 & 0 & 0 & C_3 & 0 & -C_1 \\ 0 & 0 & 0 & -C_2 & C_1 & 0 \\ 0 & -C_3 & C_2 & 0 & -C_6 & C_5 \\ C_3 & 0 & -C_1 & C_6 & 0 & -C_4 \\ -C_2 & C_1 & 0 & -C_5 & C_4 & 0 \end{pmatrix}, \quad (16)$$

where the individual elements of the matrix $\mathbf{C}_A(\mathbf{v})$ are defined as

$$C_1 = X_{\ddot{u}}u + X_{\ddot{v}}v + X_{\ddot{w}}w + X_{\ddot{p}}p + X_{\ddot{q}}q + X_{\ddot{r}}r, \quad (17)$$

$$C_2 = Y_{\ddot{u}}u + Y_{\ddot{v}}v + Y_{\ddot{w}}w + Y_{\ddot{p}}p + Y_{\ddot{q}}q + Y_{\ddot{r}}r, \quad (18)$$

$$C_3 = Z_{\ddot{u}}u + Z_{\ddot{v}}v + Z_{\ddot{w}}w + Z_{\ddot{p}}p + Z_{\ddot{q}}q + Z_{\ddot{r}}r, \quad (19)$$

$$C_4 = K_{\ddot{u}}u + K_{\ddot{v}}v + K_{\ddot{w}}w + K_{\ddot{p}}p + K_{\ddot{q}}q + K_{\ddot{r}}r, \quad (20)$$

$$C_5 = M_{\ddot{u}}u + M_{\ddot{v}}v + M_{\ddot{w}}w + M_{\ddot{p}}p + M_{\ddot{q}}q + M_{\ddot{r}}r, \quad (21)$$

$$C_6 = N_{\ddot{u}}u + N_{\ddot{v}}v + N_{\ddot{w}}w + N_{\ddot{p}}p + N_{\ddot{q}}q + N_{\ddot{r}}r. \quad (22)$$

The term $\mathbf{D}(\mathbf{v})$ represents the damping of the system that is expressed as linear damping

$$\mathbf{D}(\mathbf{v}) \approx \mathbf{D} = \begin{pmatrix} X_u & 0 & 0 & 0 & 0 & 0 \\ 0 & Y_v & 0 & Y_p & 0 & Y_r \\ 0 & 0 & Z_w & 0 & Z_q & 0 \\ 0 & K_v & 0 & K_p & 0 & K_r \\ 0 & 0 & M_w & 0 & M_q & 0 \\ 0 & N_v & 0 & N_p & 0 & N_r \end{pmatrix}, \quad (23)$$

where the coefficients X_u, Y_v, \dots, N_r are known as hydrodynamic derivatives. There are several causes of the damping – potential damping, surface friction, wave drift damping, damping due to vortex shedding, and lifting forces.

It is assumed that gravitational forces and torques $\mathbf{g}(\boldsymbol{\eta})$, also called restoring forces, are zero in equilibrium position $z = 0$, in which nominal water volume is displaced by the USV. The function $\mathbf{g}(\boldsymbol{\eta})$ is rewritten using linear approximation as

$$\mathbf{g}(\boldsymbol{\eta}) \approx \mathbf{G}\boldsymbol{\eta}, \quad (24)$$

where matrix \mathbf{G} has the following form

$$\mathbf{G} = \begin{pmatrix} 0 & 0 & 0 & 0 & 0 & 0 \\ 0 & 0 & 0 & 0 & 0 & 0 \\ 0 & 0 & -Z_z & 0 & -Z_\theta & 0 \\ 0 & 0 & 0 & -K_\phi & 0 & 0 \\ 0 & 0 & -M_z & 0 & -M_\theta & 0 \\ 0 & 0 & 0 & 0 & 0 & 0 \end{pmatrix}, \quad (25)$$

and $Z_z, Z_\theta, K_\phi, M_z$, and M_θ are the gravitational coefficients.

The modeling and measurement of the vector of forces $\boldsymbol{\tau}$ acting on the USV are challenging. The effects of waves are presented in Section 4, as it is one of the main challenges for the state estimation approach designed in this paper. Assuming that there are no acting forces $\boldsymbol{\tau}$, the nonlinear model of the USV is expressed as

$$\dot{\boldsymbol{\eta}} = \mathbf{J}(\boldsymbol{\eta})\mathbf{v}, \quad (26)$$

$$\dot{\mathbf{v}} = \mathbf{M}^{-1}(-\mathbf{C}(\mathbf{v})\mathbf{v} - \mathbf{D}\mathbf{v} - \mathbf{G}\boldsymbol{\eta}). \quad (27)$$

3.3. Linear USV model

The nonlinear USV state space model defined in (26) and (27) is linearized under the following assumptions. Firstly, the roll angle ϕ and pitch angle θ are assumed to be small. This assumption also holds for a USV whose roll and pitch

motions are limited. The (26) is reformulated using the first assumption as

$$\dot{\boldsymbol{\eta}} = \mathbf{J}(\boldsymbol{\eta})\mathbf{v} \stackrel{\phi=\theta=0}{\approx} \mathbf{J}_\psi(\psi)\mathbf{v}, \quad (28)$$

where transformation matrix $\mathbf{J}_\psi(\psi)$ is

$$\mathbf{J}_\psi(\psi) = \begin{pmatrix} \mathbf{R}_\psi & \mathbf{O}_{3 \times 3} \\ \mathbf{O}_{3 \times 3} & \mathbf{I}_{3 \times 3} \end{pmatrix}. \quad (29)$$

Using (28), the *Vessel parallel coordinate system* is defined as

$$\boldsymbol{\eta}_L = \mathbf{J}_\psi^\top(\psi)\boldsymbol{\eta}, \quad (30)$$

where $\boldsymbol{\eta}_L$ denotes the position and orientation in the global coordinate frame expressed in the body-fixed coordinate frame and $\mathbf{J}_\psi^\top(\psi)\mathbf{J}_\psi(\psi) = \mathbf{I}_{6 \times 6}$. The time derivative of $\boldsymbol{\eta}_L$ is expressed as

$$\dot{\boldsymbol{\eta}}_L = \dot{\mathbf{J}}_\psi^\top(\psi)\boldsymbol{\eta} + \mathbf{J}_\psi^\top(\psi)\dot{\boldsymbol{\eta}}. \quad (31)$$

After substitution of the term $\boldsymbol{\eta} = \mathbf{J}_\psi(\psi)\boldsymbol{\eta}_L$ and $\dot{\boldsymbol{\eta}} \approx \mathbf{J}_\psi(\psi)\mathbf{v}$, the equation (31) becomes

$$\dot{\boldsymbol{\eta}}_L = \dot{\mathbf{J}}_\psi^\top(\psi)\mathbf{J}_\psi(\psi)\boldsymbol{\eta}_L + \mathbf{J}_\psi^\top(\psi)\mathbf{J}_\psi(\psi)\mathbf{v} = r\mathbf{S}\boldsymbol{\eta}_L + \mathbf{v}, \quad (32)$$

where r is the yaw angular velocity and

$$\mathbf{S} = \begin{pmatrix} 0 & 1 & 0 & 0 & 0 & 0 \\ -1 & 0 & 0 & 0 & 0 & 0 \\ 0 & 0 & 0 & 0 & 0 & 0 \\ 0 & 0 & 0 & 0 & 0 & 0 \\ 0 & 0 & 0 & 0 & 0 & 0 \\ 0 & 0 & 0 & 0 & 0 & 0 \end{pmatrix}. \quad (33)$$

Considering $r \approx 0$, the equation (32) is as

$$\dot{\boldsymbol{\eta}}_L \approx \mathbf{v}. \quad (34)$$

The term $\mathbf{G}\boldsymbol{\eta}$ (24) representing the gravitational and buoyancy forces is also expressed using the Vessel parallel coordinate system as

$$\mathbf{G}\boldsymbol{\eta} \stackrel{\phi=\theta=0}{\approx} \mathbf{G}\boldsymbol{\eta}_L. \quad (35)$$

The nonlinear damping term $\mathbf{D}(\mathbf{v})$ is converted to a linear form as presented in (23). The last nonlinear term represents Coriolis and centripetal forces $\mathbf{C}(\mathbf{v})$. Assuming that $\phi = \theta = 0$ and that, in low-speed applications, $\mathbf{v} \approx \mathbf{0}$, the term $\mathbf{C}(\mathbf{v})$ becomes the zero matrix $\mathbf{C}(\mathbf{v}) = \mathbf{O}_{6 \times 6}$. Finally, the nonlinear state space equations (26) and (27) are transformed into a linear form as

$$\dot{\boldsymbol{\eta}}_L = \mathbf{v}, \quad (36)$$

$$\dot{\mathbf{v}} = -\mathbf{M}^{-1}\mathbf{D}\mathbf{v} - \mathbf{M}^{-1}\mathbf{G}\boldsymbol{\eta}_L. \quad (37)$$

The Linear time-invariant (LTI) state space model is expressed as

$$\dot{\mathbf{x}}_{vp} = \mathbf{A}_{vp}\mathbf{x}_{vp}, \quad (38)$$

where $\mathbf{x}_{vp} = (\boldsymbol{\eta}_L^\top, \mathbf{v}^\top)^\top$ and

$$\mathbf{A}_{vp} = \begin{pmatrix} \mathbf{O}_{6 \times 6} & \mathbf{I}_{6 \times 6} \\ -\mathbf{M}^{-1}\mathbf{G} & -\mathbf{M}^{-1}\mathbf{D} \end{pmatrix}. \quad (39)$$

The global position $\boldsymbol{\eta}$ is computed from $\boldsymbol{\eta}_L$ as

$$\boldsymbol{\eta} = \mathbf{J}_\psi(\psi)\boldsymbol{\eta}_L. \quad (40)$$

4. WAVE MODEL

The motion of the USV is significantly influenced by the wave forces. The results of their actions are oscillatory motions with a zero mean Fossen (2011). Under frequency decomposition, the wave elevation at time t is expressed as a sum of $N \in \mathbb{Z}^+$ harmonic components

$$\zeta(t) = \sum_{k=1}^N A_k \cos(\omega_k t + \epsilon_k), \quad (41)$$

where A_k is the amplitude of the wave component k , ω_k denotes the frequency of wave component k , and ϵ_k is a random phase angle of wave component k . The characteristics of waves are captured in their spectrum $S(\omega_k)$ Fossen (2011). The amplitude A_k of wave component k is related to the wave spectrum $S(\omega_k)$ as

$$\frac{1}{2}A_k^2 = S(\omega_k)\Delta\omega_k, \quad (42)$$

where $\Delta\omega_k$ denotes a constant difference between the frequencies of wave components k and $k-1$.

To use wave elevation in the nonlinear USV model, a system generating the harmonic signal as one wave component is needed. We propose to design the system of one wave component as

$$\dot{x}_{\omega_{N1}} = x_{\omega_{N2}}, \quad (43)$$

$$\dot{x}_{\omega_{N2}} = -x_{\omega_{N3}} \sin(x_{\omega_{N1}}) - \gamma x_{\omega_{N2}}, \quad (44)$$

$$\dot{x}_{\omega_{N3}} = 0, \quad (45)$$

$$y_{\omega_N} = x_{\omega_{N2}}, \quad (46)$$

where $x_{\omega_{N1}}$, $x_{\omega_{N2}}$, and $x_{\omega_{N3}}$ are state variables of the system, y_{ω_N} is an output signal of one wave component, and γ is a damping term of the wave component. The state $x_{\omega_{N3}}$ corresponds to the frequency of the wave component that does not evolve in time. The system defined by equations (43)–(46) is expressed using $\mathbf{x}_{\omega_N} = (x_{\omega_{N1}}, x_{\omega_{N2}}, x_{\omega_{N3}})^\top$ as

$$\dot{\mathbf{x}}_{\omega_N} = \mathbf{f}_{\omega_N}(\mathbf{x}_{\omega_N}), \quad (47)$$

$$y_{\omega_N} = \mathbf{g}_{\omega_N}(\mathbf{x}_{\omega_N}). \quad (48)$$

The $N_{nc} \in \mathbb{Z}^+$ individual components y_{ω_N} defined in (48) are summed together to obtain the complex wave motion

$$\dot{\mathbf{x}}_{\omega_{N1}} = \mathbf{f}_{\omega_N}(\mathbf{x}_{\omega_{N1}}), \quad (49)$$

$$y_{\omega_{N1}} = \mathbf{g}_{\omega_N}(\mathbf{x}_{\omega_{N1}}), \quad (50)$$

$$\begin{aligned} & \vdots \\ \dot{\mathbf{x}}_{\omega_{NN_{nc}}} &= \mathbf{f}_{\omega_N}(\mathbf{x}_{\omega_{NN_{nc}}}), \end{aligned} \quad (51)$$

$$y_{\omega_{NN_{nc}}} = \mathbf{g}_{\omega_N}(\mathbf{x}_{\omega_{NN_{nc}}}), \quad (52)$$

$$y_{wave} = y_{\omega_{N1}} + \dots + y_{\omega_{NN_{nc}}}, \quad (53)$$

which is simplified using a new state $\mathbf{x}_{wave} = (\mathbf{x}_{\omega_{N1}}^T, \dots, \mathbf{x}_{\omega_{NN_{nc}}}^T)^T$ into

$$\dot{\mathbf{x}}_{wave} = \mathbf{f}_{wave}(\mathbf{x}_{wave}), \quad (54)$$

$$y_{wave} = \mathbf{g}_{wave}(\mathbf{x}_{wave}). \quad (55)$$

The y_{wave} (55) is used to create a new state vector \mathbf{v}_{wave} as

$$\mathbf{v}_{wave} = (y_{wave,u}, y_{wave,v}, y_{wave,w}, \quad (56)$$

$$y_{wave,p}, y_{wave,q}, y_{wave,r})^T, \quad (57)$$

where each element $y_{wave,u}, y_{wave,v}, y_{wave,w}, y_{wave,p}, y_{wave,q}, y_{wave,r}$ corresponds to a one wave system defined in (54) and (55). Finally, we propose the novel nonlinear 6 DOF model of the USV containing wave dynamics as

$$\dot{\boldsymbol{\eta}} = \mathbf{J}(\boldsymbol{\eta})\mathbf{v}, \quad (58)$$

$$\dot{\mathbf{v}} = \mathbf{M}^{-1}(-\mathbf{C}(\mathbf{v})\mathbf{v} - \mathbf{D}(\mathbf{v})\mathbf{v} - \mathbf{G}\boldsymbol{\eta}) + \mathbf{v}_{wave}, \quad (59)$$

$$\dot{\mathbf{x}}_{wave,u} = \mathbf{f}_{wave}(\mathbf{x}_{wave,u}), \quad (60)$$

$$\dot{\mathbf{x}}_{wave,v} = \mathbf{f}_{wave}(\mathbf{x}_{wave,v}), \quad (61)$$

$$\dot{\mathbf{x}}_{wave,w} = \mathbf{f}_{wave}(\mathbf{x}_{wave,w}), \quad (62)$$

$$\dot{\mathbf{x}}_{wave,p} = \mathbf{f}_{wave}(\mathbf{x}_{wave,p}), \quad (63)$$

$$\dot{\mathbf{x}}_{wave,q} = \mathbf{f}_{wave}(\mathbf{x}_{wave,q}), \quad (64)$$

$$\dot{\mathbf{x}}_{wave,r} = \mathbf{f}_{wave}(\mathbf{x}_{wave,r}). \quad (65)$$

Let us define

$$\mathbf{x}_{USV} = (\boldsymbol{\eta}^T, \mathbf{v}^T, \mathbf{x}_{wave,u}^T, \dots, \mathbf{x}_{wave,r}^T)^T. \quad (66)$$

Then the nonlinear model of the USV defined in (58)–(65) is written as

$$\dot{\mathbf{x}}_{USV} = \mathbf{f}_{USV}(\mathbf{x}_{USV}). \quad (67)$$

The wave system defined in (54) and (55) cannot be used for the linear USV model as the wave system is nonlinear. Therefore, we present the linear state-space model of a one wave component including two states $x_{\omega_{L1}}, x_{\omega_{L2}}$ as follows:

$$\begin{pmatrix} \dot{x}_{\omega_{L1}} \\ \dot{x}_{\omega_{L2}} \end{pmatrix} = \begin{pmatrix} 0 & 1 \\ -\omega_{0L}^2 & -2\lambda_L\omega_{0L} \end{pmatrix} \begin{pmatrix} x_{\omega_{L1}} \\ x_{\omega_{L2}} \end{pmatrix}, \quad (68)$$

$$y_{\omega_L} = \begin{pmatrix} 0 & 1 \end{pmatrix} \begin{pmatrix} x_{\omega_{L1}} \\ x_{\omega_{L2}} \end{pmatrix}, \quad (69)$$

where ω_{0L} represents the frequency of the wave component and λ_L is the damping of the wave component. The wave component defined in (68) and (69) is expressed in matrix form as

$$\dot{\mathbf{x}}_{\omega_L} = \mathbf{A}_{\omega_L} \mathbf{x}_{\omega_L}, \quad (70)$$

$$y_{\omega_L} = \mathbf{C}_{\omega_L} \mathbf{x}_{\omega_L}. \quad (71)$$

To achieve complex wave motion composed of several harmonics, the $N_{lc} \in \mathbb{Z}^+$ state-space wave components y_{ω_L} can be joined together with different parameters ω_{0L} and λ_L as

$$\dot{\mathbf{x}}_{\omega_{L1}} = \mathbf{A}_{\omega_{L1}} \mathbf{x}_{\omega_{L1}}, \quad (72)$$

$$y_{\omega_{L1}} = \mathbf{C}_{\omega_{L1}} \mathbf{x}_{\omega_{L1}}, \quad (73)$$

\vdots

$$\dot{\mathbf{x}}_{\omega_{LN_{lc}}} = \mathbf{A}_{\omega_{LN_{lc}}} \mathbf{x}_{\omega_{LN_{lc}}}, \quad (74)$$

$$y_{\omega_{LN_{lc}}} = \mathbf{C}_{\omega_{LN_{lc}}} \mathbf{x}_{\omega_{LN_{lc}}}, \quad (75)$$

$$y_{wave_L} = y_{\omega_{L1}} + \dots + y_{\omega_{LN_{lc}}}. \quad (76)$$

The system described in (72)–(76) is expressed as one linear system

$$\dot{\mathbf{x}}_{wave_L} = \mathbf{A}_{wave_L} \mathbf{x}_{wave_L}, \quad (77)$$

$$y_{wave_L} = \mathbf{C}_{wave_L} \mathbf{x}_{wave_L}, \quad (78)$$

where

$$\mathbf{x}_{wave_L} = (\mathbf{x}_{\omega_{L1}}^T, \dots, \mathbf{x}_{\omega_{LN_{lc}}}^T)^T, \quad (79)$$

$$\mathbf{A}_{wave_L} = \text{diag}\{\mathbf{A}_{\omega_{L1}}, \dots, \mathbf{A}_{\omega_{LN_{lc}}}\}, \quad (80)$$

$$\mathbf{C}_{wave_L} = \begin{pmatrix} \mathbf{C}_{\omega_{L1}} & \dots & \mathbf{C}_{\omega_{LN_{lc}}} \end{pmatrix}. \quad (81)$$

In (80) $\text{diag}\{\cdot\}$ represents a block diagonal matrix of the given elements $\mathbf{A}_{\omega_{L1}}, \dots, \mathbf{A}_{\omega_{LN_{lc}}}$.

The one wave system in (77) and (78) influences one USV state of \mathbf{v} (2). Therefore, we propose the complex wave system for the USV states \mathbf{v} as

$$\dot{\mathbf{x}}_{wave,\mathbf{v}} = \mathbf{A}_{wave,\mathbf{v}} \mathbf{x}_{wave,\mathbf{v}}, \quad (82)$$

$$y_{wave,\mathbf{v}} = \mathbf{C}_{wave,\mathbf{v}} \mathbf{x}_{wave,\mathbf{v}}, \quad (83)$$

$$\mathbf{A}_{wave,\mathbf{v}} = \text{diag}\{\mathbf{A}_{wave_L}, \mathbf{A}_{wave_L}, \mathbf{A}_{wave_L}, \mathbf{A}_{wave_L}, \mathbf{A}_{wave_L}, \mathbf{A}_{wave_L}\}, \quad (84)$$

$$\mathbf{C}_{wave,\mathbf{v}} = \begin{pmatrix} \mathbf{C}_{wave_L} & \mathbf{O}_{1 \times 2N_{lc}} & \mathbf{O}_{1 \times 2N_{lc}} \\ \mathbf{O}_{1 \times 2N_{lc}} & \mathbf{C}_{wave_L} & \mathbf{O}_{1 \times 2N_{lc}} \\ \mathbf{O}_{1 \times 2N_{lc}} & \mathbf{O}_{1 \times 2N_{lc}} & \mathbf{C}_{wave_L} \\ \mathbf{O}_{1 \times 2N_{lc}} & \mathbf{O}_{1 \times 2N_{lc}} & \mathbf{O}_{1 \times 2N_{lc}} \\ \mathbf{O}_{1 \times 2N_{lc}} & \mathbf{O}_{1 \times 2N_{lc}} & \mathbf{O}_{1 \times 2N_{lc}} \\ \mathbf{O}_{1 \times 2N_{lc}} & \mathbf{O}_{1 \times 2N_{lc}} & \mathbf{O}_{1 \times 2N_{lc}} \end{pmatrix}, \quad (85)$$

where $\mathbf{A}_{wave,\mathbf{v}}$ is a block diagonal matrix of this complex wave system and

$$\mathbf{x}_{wave,\mathbf{v}} = (\mathbf{x}_{wave_L,u}^T, \mathbf{x}_{wave_L,v}^T, \mathbf{x}_{wave_L,w}^T, \mathbf{x}_{wave_L,p}^T, \mathbf{x}_{wave_L,q}^T, \mathbf{x}_{wave_L,r}^T)^T. \quad (86)$$

We present a linear 6 DOF model of the USV containing wave dynamics (82)-(85) as

$$\dot{\mathbf{x}}_{L,usv} = \mathbf{A}_{L,usv} \mathbf{x}_{L,usv}, \quad (87)$$

where $\mathbf{x}_{L,usv} = (\eta_L^T, \mathbf{v}^T, \mathbf{x}_{wave,v}^T)^T$ and

$$\mathbf{A}_{L,usv} = \begin{pmatrix} \mathbf{O}_{6 \times 6} & \mathbf{I}_{6 \times 6} & \mathbf{O}_{6 \times 12N_{lc}} \\ -\mathbf{M}^{-1}\mathbf{G} & -\mathbf{M}^{-1}\mathbf{D} & \mathbf{C}_{wave,v} \\ \mathbf{O}_{12N_{lc} \times 6} & \mathbf{O}_{12N_{lc} \times 6} & \mathbf{A}_{wave,v} \end{pmatrix}. \quad (88)$$

4.1. State estimator

The Unscented Kalman Filter (UKF) Julier and Uhlmann (1997) with the novel nonlinear USV model (67) was selected as a state estimator. The main advantage of this filter is that no linearization step is required. The filter uses a nonlinear model of system dynamics, as well as nonlinear models of sensors, and consists of two steps:

- *prediction step* — propagate the current state and its covariance through a model of the system,
- *correction step* — use obtained measurement to update the current state and its covariance.

Moreover, the proposed novel estimation approach repeatedly applies the prediction step of the UKF to compute the desired number of predictions representing the future USV states. Firstly, the novel nonlinear mathematical USV model \mathbf{f}_{usv} defined in (67) is discretized using Runge-Kutta method of the fourth order

$$\mathbf{x}_{usv}(k_t + 1) = \mathbf{f}_{usv,d}(\mathbf{x}_{usv}(k_t), k_t), \quad (89)$$

where k_t is a discrete time step. The first predicted state $\hat{\mathbf{x}}_{usv}(0)$ and its covariance matrix $\hat{\mathbf{P}}_{usv}(0)$ are initialized by the latest estimated state $\mathbf{x}_{usv}(t_{cur})$ in time t_{cur} and its covariance matrix $\mathbf{P}_{usv}(t_{cur})$ in t_{cur}

$$\hat{\mathbf{x}}_{usv}(0) = \mathbf{x}_{usv}(t_{cur}), \quad (90)$$

$$\hat{\mathbf{P}}_{usv}(0) = \mathbf{P}_{usv}(t_{cur}). \quad (91)$$

Finally, the desired number of USV state predictions $N_{p,N} \in \mathbb{Z}^+$ is computed using the prediction step of UKF \mathbf{g}_{ukf} as

$$(\hat{\mathbf{x}}_{usv}(k_{p,N} + 1), \hat{\mathbf{P}}_{usv}(k_{p,N} + 1)) = \mathbf{g}_{ukf}(\hat{\mathbf{x}}_{usv}(k_{p,N}), \hat{\mathbf{P}}_{usv}(k_{p,N})), \quad (92)$$

where $k_{p,N} = 0, 1, \dots, N_{p,N} - 1$. The approach using UKF and the proposed novel nonlinear USV model extended by the proposed nonlinear wave model (67) is denoted as 6DOF-N in the experimental part of this paper. For comparison, we also present a linear version of the proposed approach, which uses Linear Kalman Filter (LKF) Kalman (1960) with the discrete form $\bar{\mathbf{A}}_{L,usv}$ of the linear USV model extended by a linear wave model (87), denoted as 6DOF-L. Similarly to the 6DOF-N, the prediction step of the LKF is repeatedly applied to predict desired number $N_{p,L} \in$

\mathbb{Z}^+ of future USV states $\hat{\mathbf{x}}_{L,usv}(k_{p,L})$ and corresponding covariance matrices $\hat{\mathbf{P}}_{L,usv}(k_{p,L})$

$$\hat{\mathbf{x}}_{L,usv}(k_{p,L} + 1) = \bar{\mathbf{A}}_{L,usv} \hat{\mathbf{x}}_{L,usv}(k_{p,L}), \quad (93)$$

$$\hat{\mathbf{P}}_{L,usv}(k_{p,L} + 1) = \bar{\mathbf{A}}_{L,usv} \hat{\mathbf{P}}_{L,usv}(k_{p,L}) \bar{\mathbf{A}}_{L,usv}^T + \mathbf{Q}_{L,usv}, \quad (94)$$

where $\mathbf{Q}_{L,usv} \in \mathbb{R}^{12(1+N_{lc}) \times 12(1+N_{lc})}$ is system noise matrix, $k_{p,L} = 0, 1, \dots, N_{p,L} - 1$, and the first predicted state $\hat{\mathbf{x}}_{L,usv}(0)$ and its covariance matrix $\hat{\mathbf{P}}_{L,usv}(0)$ are initialized by the latest estimated state $\mathbf{x}_{L,usv}(t_{cur})$ in time t_{cur} and its covariance matrix $\mathbf{P}_{L,usv}(t_{cur})$ in t_{cur}

$$\hat{\mathbf{x}}_{L,usv}(0) = \mathbf{x}_{L,usv}(t_{cur}), \quad (95)$$

$$\hat{\mathbf{P}}_{L,usv}(0) = \mathbf{P}_{L,usv}(t_{cur}). \quad (96)$$

5. SENSORS FOR EXPERIMENTAL EVALUATION

The Kalman filter selected as a state estimator (Section 4.1) requires sensor data obtained in real-time to estimate USV states. The sensors are divided into two groups: 1) sensors that are directly placed on the USV, 2) UAV onboard sensors. All sensor data are fused together to obtain an accurate estimation of USV states.

5.1. Sensors placed on USV

In many real-world scenarios, the UAV is at such a distance that its onboard sensors do not yield usable data for USV state estimation. However, it is assumed that the communication link between the UAV and the USV is present. To move the UAV towards the USV, the position of the USV must at least be estimated. The GNSS receiver is a widely used device to estimate the global position Abdelkrim et al. (2008); Deep et al. (2018); Kwak and Sung (2018); Lewandowski et al. (1999); Lopez (2010); Wendel et al. (2006).

The global position obtained from the GNSS receiver placed on the USV is sent to the UAV via a wireless communication link. The UAV uses this received data to roughly estimate the position of the USV. The control system takes the UAV to the proximity of the USV, where onboard sensors are used to update the estimates to be more accurate (Section 5.2). The UAV uses the received GNSS data from the USV in the correction step of the Kalman filters (Section 4.1)

Another sensor on the USV is the IMU. The IMU measures heading, angular velocity and linear acceleration. The IMU and the GPS are part of a purposely design Multi-robot Systems (MRS) boat unit within our group¹ containing the necessary electronic equipment for the USV board. A photo of the USV board is shown in Figure 5. Similar to the GPS data, the IMU data are sent to the UAV via a wireless communication link. The received IMU data are used in the correction step of the Kalman filters (Section 4.1). The motivation for adding the IMU sensor on the USV board is to

¹<http://mrs.fel.cvut.cz/>

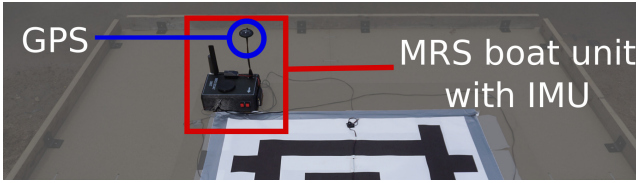


Figure 5: The GPS and the IMU placed onboard the USV.

obtain a better estimation accuracy for the motion caused by the waves (Section 4). Moreover, the combination of IMU and GPS results in a more accurate estimate of the system states — position, orientation, velocity, and angular velocity.

5.2. UAV onboard sensors

The Section 5.1 presents the sensors placed on the USV, whose data have to be sent to the UAV via a communication link. However, reliable data exchange with minimal latency between the USV and the UAV is challenging to achieve in real-world environments Tran and Ahn (2019). In order to cope with the issues of not perfect communication (Section 5.1) or USV sensors faults, the UAV is equipped with onboard vision systems that allow for direct estimation of the USV states without the need for communication or a common reference frame between the USV and the UAV. To increase the redundancy and ensure a properly working system in varying real-world conditions, two onboard sensors are used: an UltraViolet Direction And Ranging (UVDAR) system Walter et al. (2018a,b); Walter et al. (2019, 2020) and an AprilTag detector Krogus et al. (2019); Olson (2011); Wang and Olson (2016). Both vision-based systems require dedicated markers placed on the target.

The AprilTags detected by the AprilTag detector (Section 5.4) are passive reflective markers. Therefore, they are only useful under lighting conditions sufficient for imaging. If the UAV has to land in the dark, the AprilTag detector will not produce a reliable position and orientation estimation. However, the UVDAR system (Section 5.3) is able to work properly at any time of day due to the active blinking markers. Since achieving robustness is important in intended missions, we demonstrated the possibility of using two complementary onboard detection systems. Both systems are described in the Section 5.3 and 5.4.

5.3. UVDAR system

The UVDAR system is an onboard vision-based relative localization system developed by the MRS group¹ at Czech Technical University (CTU) in Prague. One of the great advantages of this system is that no communication is needed to obtain estimations of states of objects in the UAV proximity. As mentioned above, the UVDAR system requires markers placed on the target. The marker is composed of a UltraViolet (UV) LED that blinks a unique binary signal code. The blinking UV LEDs are captured by UV sensitive cameras placed onboard the UAV. The principle of the UVDAR system is presented in detail in Walter et al. (2018a,b); Walter et al. (2019, 2020).

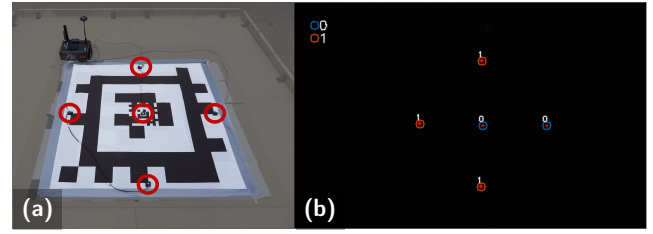


Figure 6: UV LEDs (marked with red circles) placed on the USV board (a) together with detected UV LEDs in the UV camera image (b).

The UVDAR system was originally proposed for the mutual localization of UAVs in a swarm Ahmad et al. (2021); Novak et al. (2021); Petracek et al. (2020). Therefore, a novel pattern of UV LEDs had to be defined in order to detect the horizontal landing board on the USV. We propose a 5-LED marker in the shape of a plus sign for the USV board, as shown in Figure 6. Two LEDs (with 0 sign in Figure 6 (b)) got different signal codes than the others in order to identify the orientation of the marker unambiguously. The data obtained from the UVDAR system contain relative 3D position and orientation, which is used in the correction step of the Kalman filters (Section 4.1).

5.4. AprilTag detector

The AprilTag detector is a visual fiducial system that detects artificial landmarks known as AprilTags Olson (2011); Wang and Olson (2016). A single camera with a processing unit is sufficient to detect an AprilTag on a target. The data measured by the AprilTag detector consist of the relative 3D position and orientation, which is used in the correction step of the Kalman filters (Section 4.1). The Apriltag detector supports custom tag layouts containing empty space in the middle for a recursive encapsulation of one tag in another Krogus et al. (2019); Xu et al. (2020a). This feature improves the detectability from a wide range of distances by ensuring that a tag is fully visible even from a close distance. The AprilTag layout placed on the USV board is shown in Figure 7. The custom tag layout is used, hence a smaller AprilTag is placed in the empty space of the bigger AprilTag. The size of an AprilTag configuration on a real USV board is shown in Figure 7 (b).

Although the AprilTag detector provides less noisy data in close proximity than the UVDAR system, the AprilTag detector requires sufficient light conditions for accurate AprilTag detection due to the passive markers. The proposed setup combines the AprilTag detector and UVDAR system to improve robustness and mainly show the possibility of fusing data from multiple sensors by the proposed approach. In fact, almost any relevant sensory modality can be added to both proposed approaches, 6DOF-N and 6DOF-L, if passing the innovation tests described in Section 6. As mentioned above, using these various detection approaches, we can verify the general usage of the proposed methodology, since

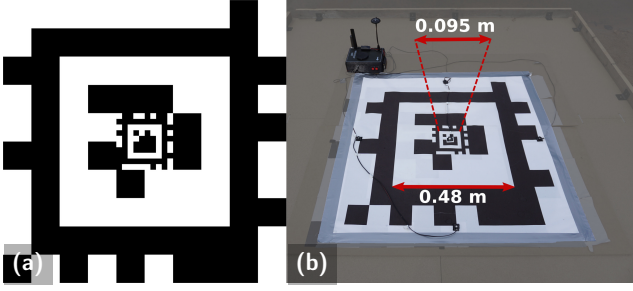


Figure 7: AprilTag layout (a) placed on the USV board (b).

almost any detection technique satisfying the later mentioned innovation tests can be integrated for the relative state estimation.

6. VERIFICATION

The estimation approach presented in this paper was integrated into the MRS system Baca et al. (2021), as shown in Figure 8. Thereafter, the estimation approach was tested in the realistic Gazebo simulator extended by the Virtual RobotX (VRX) simulator Bingham et al. (2019) (see Figure 2 (d)). It was then verified by conducting real-world experiments. The verification of the proposed approach performing state estimation is based on vector Root Mean Square Error (RMSE) Kaur and Sahambi (2016) and 3 innovation tests Evangelidis and Parker (2021); Reidr.

Innovation is defined as

$$\zeta(k) = \mathbf{y}(k) - \hat{\mathbf{y}}(k), \quad (97)$$

where $\mathbf{y}(k)$ is a measurement obtained from the sensors in time step k and $\hat{\mathbf{y}}(k)$ is the expected measurement with respect to the current estimated state. The covariance of innovation $\mathbf{S}(k)$ has the following form:

$$\mathbf{S}(k) = \mathcal{E} \{ \zeta(k) \zeta^T(k) \}, \quad (98)$$

where $\mathcal{E}\{\cdot\}$ represents the mean value of a term inside the brackets. If the filter is working correctly, then the mean of innovation $\zeta(k)$ is zero, and the matrix $\mathbf{S}(k)$ is its covariance matrix.

6.1. Test 1: Innovation magnitude bound test

The first test checks whether the innovation $\zeta(k)$ is consistent with its covariance $\mathbf{S}(k)$. According to Evangelidis and Parker (2021); Reidr, the innovation is consistent with its covariance if approximately 95% of the innovation values are within the 95% confidence ellipsoid defined by the matrix $\mathbf{S}(k)$. In the scalar case, the test means that approximately 95% of the innovation values lie within bounds $\pm 2\sqrt{\mathbf{S}(k)}$.

6.2. Test 2: Normalized innovation squared χ^2 test

The second test seeks to prove the unbiasedness of the innovation Evangelidis and Parker (2021); Reidr. To perform

the test, firstly, the normalized innovation squared $q(k)$ is determined as

$$q(k) = \zeta^T(k) \mathbf{S}^{-1}(k) \zeta(k). \quad (99)$$

Then, the mean value of $q(k)$ is computed as

$$\bar{q} = \frac{1}{N} \sum_{k=1}^N q(k). \quad (100)$$

To pass this test, the \bar{q} should lie in confidence interval $[r_1, r_2]$ characterized by the hypothesis H_0 . The hypothesis H_0 is defined as follows Reidr: $N\bar{q}$ is $\chi_{N_m}^2$ distributed with probability $P = 1 - \alpha$, where m is a dimension of the measurement vector and α defines the confidence region, e.g., $\alpha = 0.05$ specified 95% confidence region,

$$P(N\bar{q} \in [r_1, r_2] | H_0) = 1 - \alpha. \quad (101)$$

6.3. Test 3: Innovation whiteness (autocorrelation) test

The last test shows the whiteness of the innovation Reidr. The time-averaged correlation is computed during the test

$$\text{corr}(\tau) = \frac{1}{N} \sum_{k_r=0}^{N-\tau-1} \zeta(k_r)^T \zeta(k_r + \tau), \quad (102)$$

which is normalized by $\text{corr}(0)$. The idea of the test is that for a large enough N , $\text{corr}(\tau)$ is assumed to be normally distributed with zero mean and variance $\frac{1}{N}$ Reidr. Therefore, at least 95% of the values of $\text{corr}(\tau)$ should be in the confidence region defined as $\pm \frac{2}{\sqrt{N}}$.

6.4. Verification of proposed approach 6DOF-N

This section presents the verification of the proposed state estimation approach 6DOF-N (Section 4.1). The estimation of all USV states using the 6DOF-N is presented in Figure 9 and Figure 10. The estimated values nicely catch the Ground Truth (GT) data as the 6DOF-N fuses data from all sensors. The last row of Table 3 provides RMSE of the estimated USV states using the 6DOF-N computed from these experiments.

The Table 4 contains the results of the innovation tests applied to the 6DOF-N on USV states $\boldsymbol{\eta}$ (1), consisting of position x , y , z and the angles roll ϕ , pitch θ , and yaw ψ . The innovation tests are performed for individual sensors with respect to the USV states that the sensors measure. The results in Table 4 show that all sensors pass the innovation tests.

The RMSE according to the individual sensors used to estimate the desired USV states is proposed in Table 3. The largest RMSE from all sensors for states $(x, y, z)^T$ and $(u, v, w)^T$ is provided by estimation using the GPS sensor. In contrast, the estimation of the states $(\phi, \theta, \psi)^T$ and $(p, q, r)^T$ using the IMU sensor achieve the best results from all the sensors as the values of IMU RMSE for states $(\phi, \theta, \psi)^T$

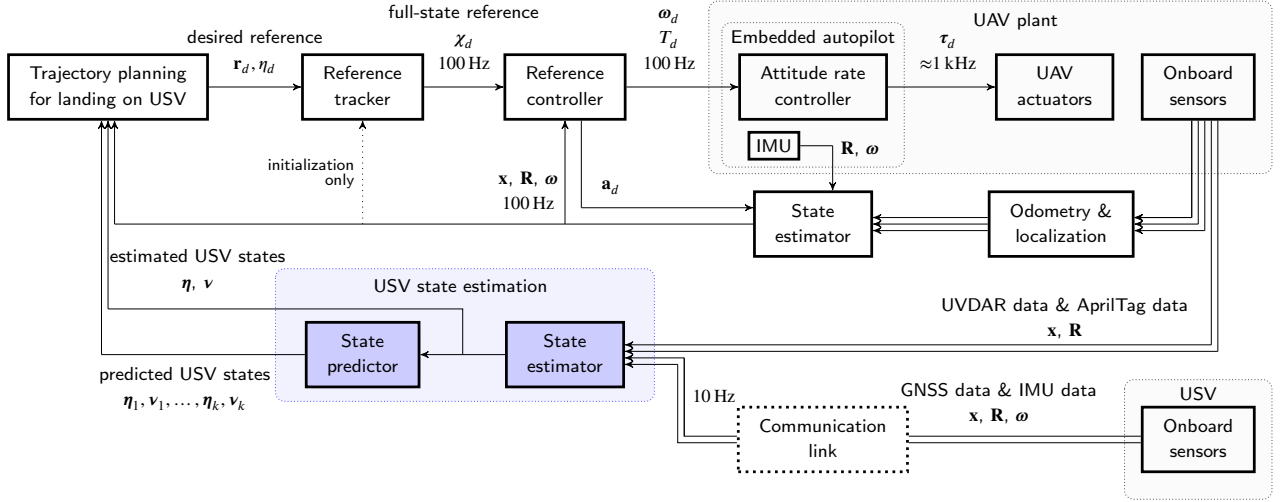


Figure 8: Pipeline diagram of the proposed USV state estimation approach presented in this paper and integrated into the MRS system Baca et al. (2021) for experimental verification in realistic robotic scenarios. *Trajectory planning for landing on USV* block computes the desired position and heading reference ($\mathbf{r}_d, \boldsymbol{\eta}_d$) for the UAV based on estimated and predicted USV states from the *USV state estimation* block. The computed trajectory is forwarded into the *Reference tracker* that converts the trajectory to a smooth and feasible reference χ_d for *Reference controller*. The *Reference controller* creates the desired thrust and angular velocities ($\boldsymbol{\omega}_d, T_d$) for the Pixhawk embedded flight controller. The *State estimator* fuses data from *Odometry & localization* block to estimate the UAV translation, rotation, and angular velocities ($\mathbf{x}, \mathbf{R}, \boldsymbol{\omega}$). The *State estimator* in *USV state estimation* block fuses data from the UAV onboard sensors (UVDAR system and AprilTag detector) and USV onboard sensors (GNSS and IMU) to estimate the USV states ($\boldsymbol{\eta}, \mathbf{v}$) using the Kalman filter. Then, the *State predictor* in *USV state estimation* block predicts the future USV states ($\boldsymbol{\eta}_1, \mathbf{v}_1, \dots, \boldsymbol{\eta}_k, \mathbf{v}_k$) based on the estimated USV states and a presented novel mathematical USV model.

sensor	RMSE (x, y, z) m	RMSE (ϕ, θ, ψ) rad	RMSE (u, v, w) m/s	RMSE (p, q, r) rad/s
GPS	0.681	-	0.837	-
IMU	-	0.011	-	0.087
UVDAR	0.289	0.123	0.385	0.248
AprilTag	0.046	0.061	0.146	0.092
all sensors	0.097	0.016	0.157	0.025

Table 3
RMSE of estimated USV states using the 6DOF-N according to the individual sensors.

sensor	states	test 1	test 2 (q of [q_{min}, q_{max}])	test 3
GPS	(x, y, z)	98.9%	2162.2 of [1998.2, 2253.6]	99.8%
IMU	(ϕ, θ, ψ)	93.1%	1040.7 of [893.2, 1066.6]	94.8%
UVDAR	(x, y, z)	96.4%	571.3 of [547.2, 684.6]	95.8%
UVDAR	(ϕ, θ, ψ)	98.4%	590.7 of [547.2, 684.6]	99.0%
AprilTag	(x, y, z)	99.1%	8568.1 of [8510.4, 9029.4]	95.3%
AprilTag	(ϕ, θ, ψ)	93.6%	8725.6 of [8510.3, 9029.4]	97.7%

Table 4
Innovation tests applied to the 6DOF-N according to the individual sensors.

and $(p, q, r)^T$ are the lowest. The estimated USV states $(x, y, z)^T$ and $(u, v, w)^T$ that use the UVDAR system have a twice smaller RMSE than states estimated by the GPS. However, the states $(\phi, \theta, \psi)^T$ estimated using the UVDAR system have a ten times greater RMSE than estimations using the IMU. The RMSE for states $(p, q, r)^T$ is three times smaller for the IMU in comparison with the UVDAR. The smallest RMSE for states $(x, y, z)^T$ and $(u, v, w)^T$ from all sensors is achieved using the AprilTag. However, the RMSE

of the AprilTag for $(\phi, \theta, \psi)^T$ is five times higher than the RMSE of the IMU. The RMSE for states $(p, q, r)^T$ using the AprilTag is slightly higher than RMSE for these states using the IMU.

The estimated states using the 6DOF-N are used to predict future USV states applying the prediction steps as described in Section 4.1. Every two seconds, the USV states are predicted for two seconds. The predicted USV states $(x, y, z, \phi, \theta, \psi)^T$ are shown in Figure 11. The graphs in Figure 11 demonstrate that the 6DOF-N is able to estimate and predict the motion of the USV.

The RMSE of states $(x, y, z)^T$ is six times larger for predicted states than for estimated ones. However, the RMSE of predicted states $(x, y, z)^T$ corresponds to the RMSE of estimated states $(x, y, z)^T$ using only the GPS sensor (Table 3). The RMSE of states $(\phi, \theta, \psi)^T$ is five times larger for predicted states than for estimated ones. The RMSE of predicted states $(\phi, \theta, \psi)^T$ is smaller than RMSE of estimated states $(\phi, \theta, \psi)^T$ using the UVDAR (Table 3). However, RMSE of predicted states $(\phi, \theta, \psi)^T$ is still larger than the RMSE of the states estimated by the AprilTag detector (Table 3).

6.5. Comparison of 6DOF-N, 6DOF-L and state-of-the-art methods

First, we compare the two proposed methods, 6DOF-N and 6DOF-L (Section 4.1). Then, we further compare both methods with the state-of-the-art. The main difference between the proposed methods is in the USV model: the

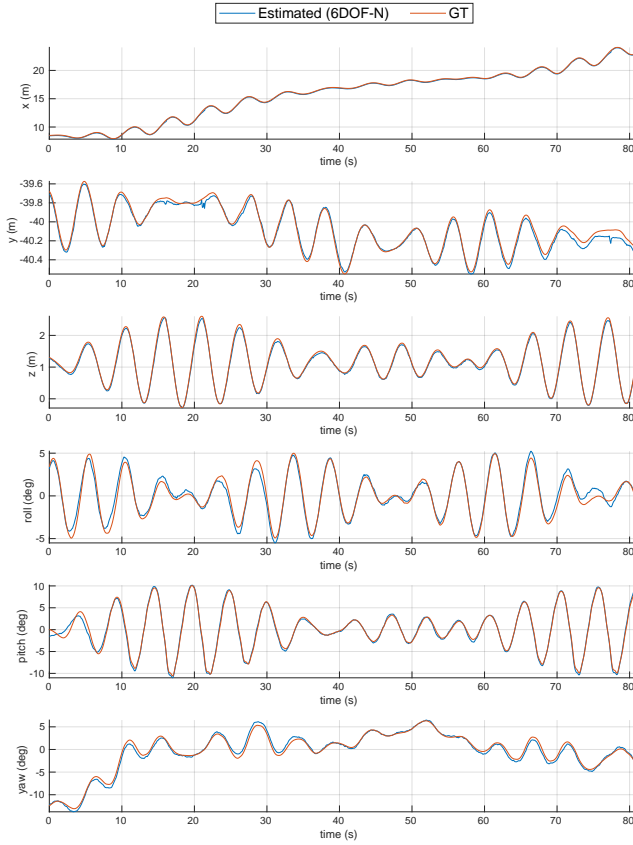


Figure 9: Estimated position $(x, y, z)^T$ and orientation $(\phi, \theta, \psi)^T$ of the USV using the 6DOF-N.

USV states	RMSE (x, y, z) m	RMSE (ϕ, θ, ψ) rad
predicted states	0.647	0.081
estimated states	0.097	0.016

Table 5

RMSE of predicted and estimated USV states using the 6DOF-N.

6DOF-N uses the nonlinear USV model extended by the nonlinear wave model (Section 3.2 and 4), while the 6DOF-L uses the linear USV model obtained by linearization of the nonlinear USV model (Section 3.3). The linear USV model is extended by the linear wave model (Section 4). The 6DOF-L benefits from using LKF as it is less computationally demanding than 6DOF-N that applies UKF on full nonlinear USV model. From our tests performed on real UAV, we found that 6DOF-L is 30% faster than 6DOF-N.

The innovation tests applied on the 6DOF-N are also performed for the 6DOF-L (Table 6). The innovation tests demonstrate that estimations using the 6DOF-L are consistent with the sensors' measurements. However, test 1 of the UVDAR system for states $(x, y, z)^T$ reaches a value 100%, but this value should be near 95%. The sensor covariance matrix $\mathbf{R}_{\text{uvdar}}$ is over-estimated in the 6DOF-L for states $(x, y, z)^T$ measured by the UVDAR system. The reason involves the high peaks in UVDAR measurements, which would negatively impact estimation. The innovation tests

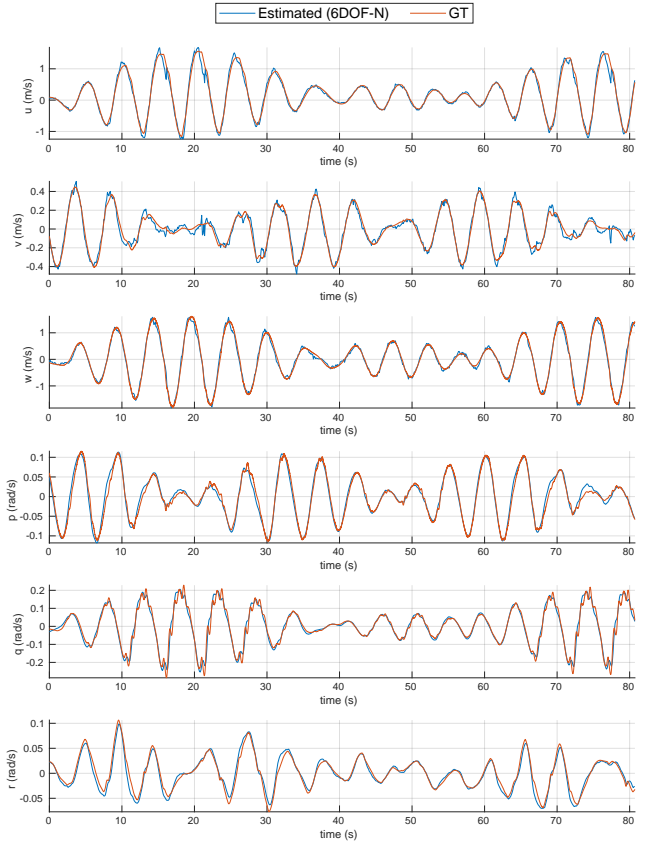


Figure 10: Estimated linear $(u, v, w)^T$ and angular $(p, q, r)^T$ velocities of the USV using the 6DOF-N.

of the 6DOF-N prove that estimations using the 6DOF-N are consistent with the sensors' measurements, even for the UVDAR system.

The RMSE of predicted states $(x, y, z)^T$ and $(\phi, \theta, \psi)^T$ using 6DOF-L is larger than RMSE of 6DOF-N (Table 7). The 6DOF-L has a 14% larger RMSE for states $(x, y, z)^T$ compared to the 6DOF-N. The RMSE of predicted states $(\phi, \theta, \psi)^T$ using 6DOF-N is two and a half times smaller than when using 6DOF-L.

The RMSE of estimated states $(u, v, w)^T$, $(p, q, r)^T$ and $(\phi, \theta, \psi)^T$ is smaller for 6DOF-N (Table 8). However, the RMSE of estimated states $(x, y, z)^T$ is slightly smaller for 6DOF-L, mainly caused by the higher computational demands of 6DOF-N compared to 6DOF-L. As mentioned above, the 6DOF-L is 30% faster than 6DOF-N. Therefore, 6DOF-L is less delayed and enables faster control loop that results in faster UAV landing and longer mission time, as spending less time on landing increases the UAV flight time. Nevertheless, for all other states, the 6DOF-N provides a more accurate estimation of the USV states because the nonlinear USV model better captures the USV motion dynamics.

In order to compare our approach with state-of-the-art methods presented in Section 2, we firstly consider works Fossen and Perez (2009); Tomera (2012); Wang et al. (2021b); Wirtensohn et al. (2016); Xu et al. (2020b) that are able to estimate the USV only with 3 DOFs, i.e. x, y and yaw

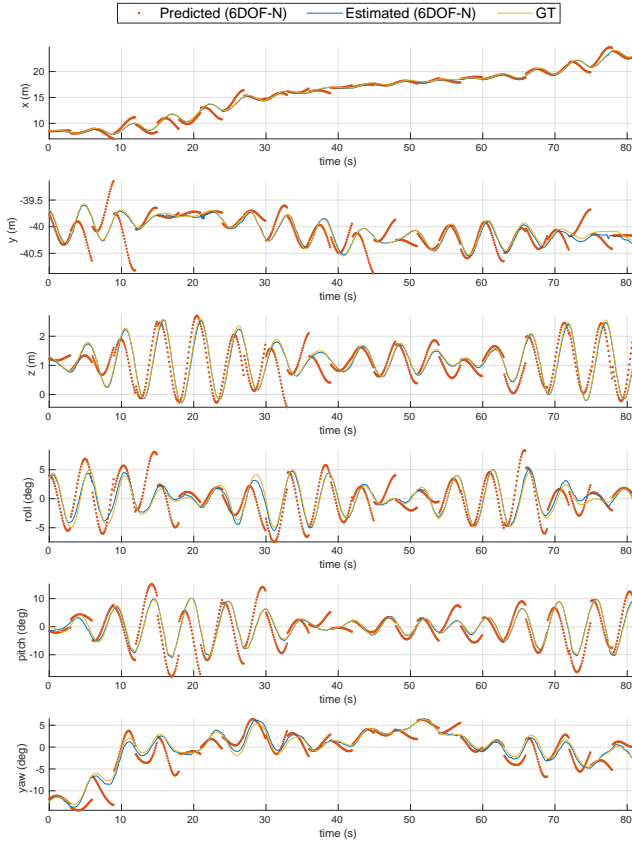


Figure 11: Predicted and estimated position $(x, y, z)^T$ and orientation $(\phi, \theta, \psi)^T$ of the USV using the 6DOF-N.

sensor	states	test 1	test 2	test 3
			(q of $[q_{min}, q_{max}]$)	
GPS	(x, y, z)	98.2%	644.7 of [590.7, 733.1]	99.7%
IMU	(ϕ, θ, ψ)	93.7%	1008.7 of [866.5, 1037.3]	98.5%
UVDAR	(x, y, z)	100%	683.6 of [824.5, 991.3]	96.9%
UVDAR	(ϕ, θ, ψ)	96.5%	830.4 of [824.5, 991.3]	99.3%
AprilTag	(x, y, z)	96.7%	8701.4 of [8486.7, 9005.1]	97.3%
AprilTag	(ϕ, θ, ψ)	95.5%	8800.2 of [8486.7, 9005.1]	98.5%

Table 6

Innovation tests applied to the 6DOF-L according to the individual sensors.

predicted USV states	RMSE	RMSE
	(x, y, z) m	(ϕ, θ, ψ) rad
6DOF-N	0.647	0.081
6DOF-L	0.737	0.196

Table 7

RMSE of predicted USV states using the 6DOF-N and 6DOF-L.

angle. Therefore no information about z (heave) position and roll and pitch angles are provided. However, these states have a significant influence on USV motion relatively to the UAV as seen in Figure 9 and Figure 10. Not considering these states during autonomous landing can lead to unsafe maneuvers or crashes, as shown in Figure 2 (a) where a heave motion of a ship damages a landing helicopter. We observed the same problems in our initial simulations, and due to the

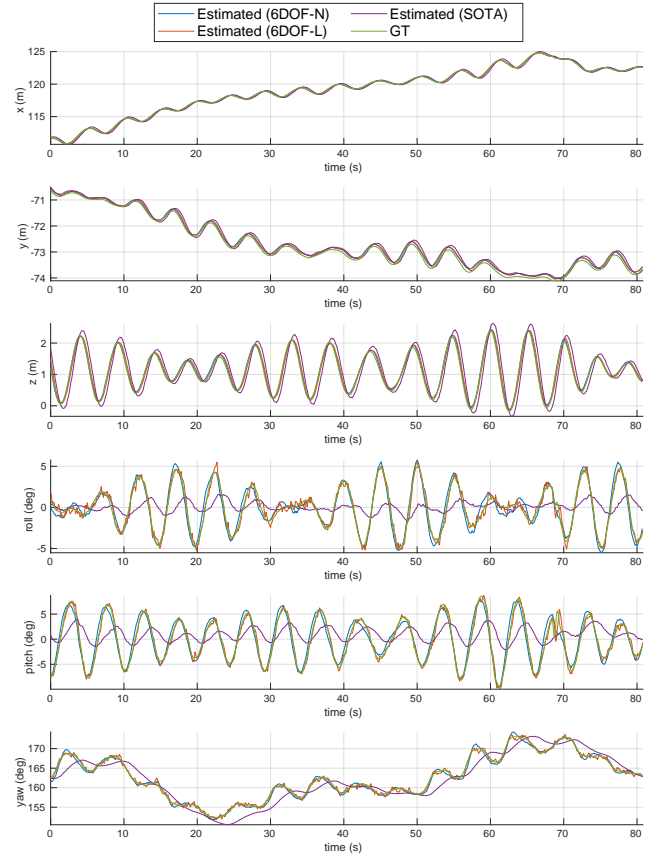


Figure 12: Estimated position $(x, y, z)^T$ and orientation $(\phi, \theta, \psi)^T$ of the USV using the 6DOF-N, 6DOF-L and state-of-the-art method (SOTA).

sensor	RMSE	RMSE	RMSE	RMSE
	(x, y, z) m	(ϕ, θ, ψ) rad	(u, v, w) m/s	(p, q, r) rad/s
6DOF-N	0.120	0.013	0.201	0.204
6DOF-L	0.116	0.017	0.303	0.235
SOTA	0.313	0.056	0.580	0.329

Table 8

RMSE of estimated USV states using the 6DOF-N, 6DOF-L and state-of-the-art method (SOTA).

high rise of collision, we could not repeat the evaluation in real-world conditions using these 3 DOF approaches.

Therefore, we present a comparison of USV state estimation with 6 DOFs between proposed approaches 6DOF-N and 6DOF-L and state-of-the-art method Polvara et al. (2018), which we call SOTA. The approach Abujoub et al. (2018) is very similar to the SOTA method Polvara et al. (2018), however, the Abujoub et al. (2018) uses only 5 DOFs. The Figure 12 shows estimated position $(x, y, z)^T$ and orientation $(\phi, \theta, \psi)^T$. The SOTA had a non-negligible problem in estimating wave motions in orientation and also incorrectly estimated a larger amplitude in state z together with a larger delay than the proposed approaches 6DOF-N and 6DOF-L. The better performance of proposed approaches 6DOF-N and 6DOF-L compared to SOTA is demonstrated by the RMSE values presented in Table 8.

The RMSE of SOTA is the largest for all USV states $(x, y, z)^T$, $(\phi, \theta, \psi)^T$, $(u, v, w)^T$, and $(p, q, r)^T$ compared to the 6DOF-N and 6DOF-L. The biggest difference is in estimation of orientation $(\phi, \theta, \psi)^T$, as the SOTA has the RMSE three times larger than 6DOF-N and 6DOF-L.

7. REAL-WORLD EXPERIMENTS

After a successful verification in the realistic robotic simulator Gazebo, the estimation approach presented in this paper was deployed in real-world experiments. Multimedia materials supporting the results of this paper are available at <https://mrs.fel.cvut.cz/papers/usv-state-estimation>. Numerous real-world experiments were performed, with two of them representing two different application scenarios presented in this section. Firstly, the UAV followed the moving USV with artificially-induced wave motion. Secondly, the UAV took off and flew above the USV. Then, the UAV followed the moving USV using estimated and predicted states of the USV. During the USV following, the UAV used the predicted USV states to select the moment for landing. Finally, the UAV landed on the estimated landing platform located on the USV.

The UAV used in real-world experiments is presented in Figure 13 (a) (see Hert et al. (2023, 2022) for details about our hardware equipment). The UAV is equipped with the necessary sensors for the estimation of USV states — the RealSense camera for the AprilTag detector and the UVDAR camera for the UVDAR system. The UAV also carries a GPS receiver for obtaining its position in GPS coordinates. It is further used to include the incoming USV GPS data with the estimation system of the USV states. The Figure 13 (b) shows the USV landing platform used in real-world experiments. The AprilTag is centered on the USV board (Section 5.4). The four UV LEDs are located around the perimeter of the AprilTag, and one UV LED is placed in the center of the AprilTag (Section 5.3). The MRS boat unit is installed next to the AprilTag and contains a GPS module and a IMU sensor (Section 5.1).

In the first real-world scenario, the UAV followed the moving USV (see video²). The Figure 14 presents the estimated USV states x , y , z , roll ϕ , pitch θ , and yaw ψ in one of the experimental flights using the proposed approaches

²<https://mrs.fel.cvut.cz/papers/usv-state-estimation>

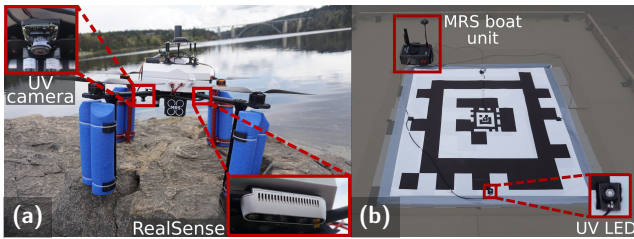


Figure 13: The UAV (a) and USV landing platform (b) used in real-world experiments.

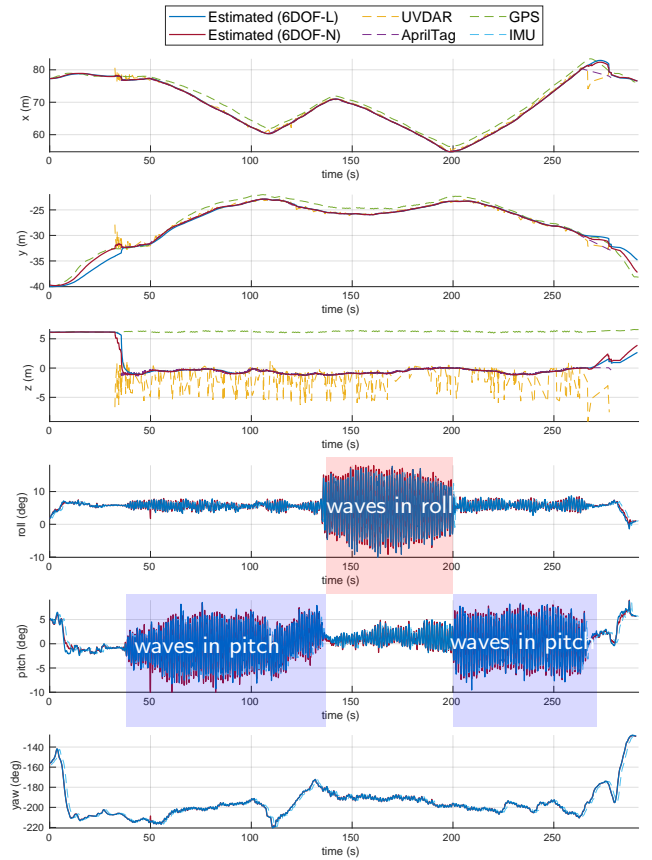


Figure 14: Estimation of the USV states $(x, y, z, \phi, \theta, \psi)^T$ obtained using the 6DOF-L and the 6DOF-N while the UAV was following the moving and oscillating USV.

6DOF-L and 6DOF-N (Section 4.1). The UAV onboard sensors provided the first data at time $t = 30$ s that improved the estimation of the USV states, especially in the z position. The graphs of roll ϕ and pitch θ contain wave motions marked in the Figure 14. Both approaches 6DOF-L and 6DOF-N captured these motions in their estimations. The graphs of roll, pitch, and yaw do not contain the UVDAR and AprilTag measurements as these measurements are very noisy.

In the second scenario, the UAV flew above the USV and estimated the USV states using only the data received from the USV onboard sensors — the GPS and the IMU. We provide data from one of the experimental flights in Figure 15. After the UAV onboard sensors (UVDAR system and AprilTag detector) detected the desired markers in their camera frames, the measurements from these UAV onboard sensors improved the estimations of the USV states. The UAV followed the moving USV for 98 s using the estimated and predicted USV states. While following the USV, the UAV was looking for acceptable conditions to land on the USV and canceled the landing maneuver whenever the landing was unsafe for the UAV. At time $t = 142$ s, the UAV successfully landed on the USV (see video²).

The estimations of the USV states from the proposed approaches 6DOF-L and 6DOF-N during this real-world

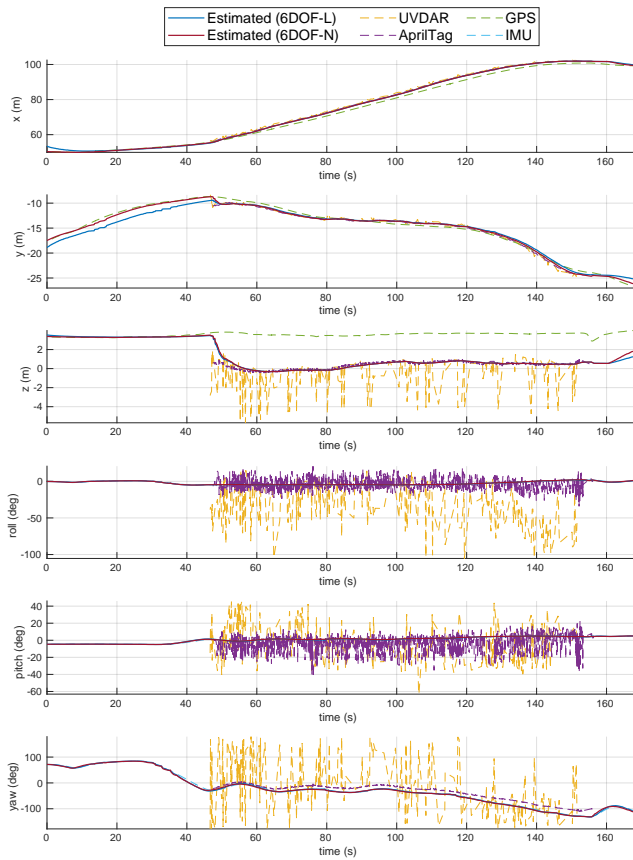


Figure 15: Estimation of the USV states $(x, y, z, \phi, \theta, \psi)^T$ using the 6DOF-L and 6DOF-N while the UAV followed the USV and then landed on it.

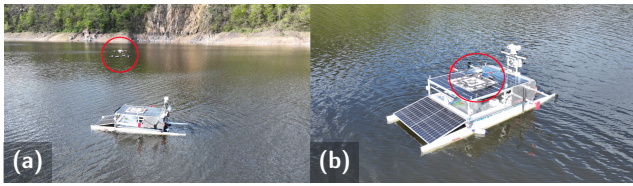


Figure 16: Snapshots from the real-world experiment in which the UAV followed the USV (a). The experiment was finished with a successful landing (b).

experiment are presented in Figure 15. The UAV onboard sensors began providing data at time $t = 45$ s and improved estimation of the USV states; this is prevalent especially in the graph of the USV state z . The UVDAR measurements of z , roll ϕ , pitch θ , yaw ψ , and the AprilTag measurements of roll ψ and pitch θ were very noisy. However, the 6DOF-L and 6DOF-N filtered the noise out and were able to provide a smooth estimation of the USV states. The snapshots from one of these real-world experiments are shown in Figure 16. The reliability and practical usefulness of the proposed approach were also demonstrated during the testing of a high-tech system of cooperating UAV-USV designed for quality water monitoring and garbage removal (see Figure 17).

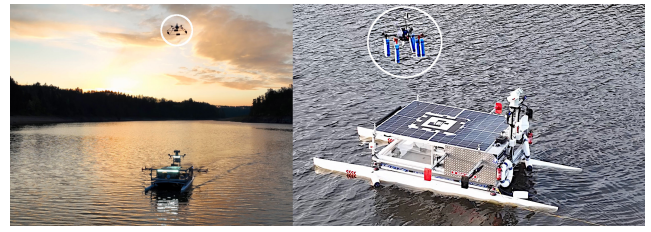


Figure 17: Snapshot from testing of the proposed approach integrated into a complex system of water-proofed floatable UAV and fully autonomous USV cooperating in various real-world conditions.

8. CONCLUSION

This paper presents a novel approach for the state estimation and prediction of a USV moving on a rough water surface. This work introduces a novel nonlinear model of the USV in 6 DOFs extended by wave motion dynamics tailored for UAV-USV tight collaboration. The usage of the USV mathematical model allows for estimating all 6 DOF states of the USV moving in waves, and also predicting the future USV states including wave motions. In order to achieve the required reliability, the estimation pipeline is able to fuse data from multiple sensors. Thus, the presented approach is capable of being used in different real-world conditions and at varying distances between the UAV and the USV. The performance of estimation and prediction was exhaustively verified in simulations and was compared with state-of-the-art methods. The comparison with the state-of-the-art methods demonstrated that the proposed approach significantly surpassed these methods. Finally, the approach integrated into a complex UAV-USV system was deployed and experimentally verified in real-world conditions, where the UAV was successfully following the USV and repeatably landing on its landing deck.

References

- Abdelkrim, N., Aouf, N., Tsourdos, A., White, B., 2008. Robust nonlinear filtering for INS/GPS UAV localization, in: 2008 16th Mediterranean Conference on Control and Automation, pp. 695–702. doi:10.1109/MED.2008.4602149.
- Abujoub, S., McPhee, J., Westin, C., Irani, R.A., 2018. Unmanned aerial vehicle landing on maritime vessels using signal prediction of the ship motion, in: OCEANS 2018 MTS/IEEE Charleston, pp. 1–9. doi:10.1109/OCEANS.2018.8604820.
- Ahmad, A., Walter, V., Petracek, P., Petrlik, M., Baca, T., Zaitlik, D., Saska, M., 2021. Autonomous aerial swarming in GNSS-denied environments with high obstacle density, in: 2021 IEEE International Conference on Robotics and Automation (ICRA), IEEE. pp. 570–576. doi:10.1109/ICRA48506.2021.9561284.
- Aissi, M., Moumen, Y., Berrich, J., Bouchentouf, T., Bourhaleb, M., Rahmoun, M., 2020. Autonomous solar USV with an automated launch and recovery system for UAV: State of the art and design, in: 2020 IEEE 2nd International Conference on Electronics, Control, Optimization and Computer Science (ICECOCS), pp. 1–6. doi:10.1109/ICECOCS50124.2020.9314415.
- Assaf, M.H., Petriu, E.M., Groza, V., 2018. Ship track estimation using GPS data and Kalman filter, in: 2018 IEEE International Instrumentation and Measurement Technology Conference (I2MTC), pp. 1–6. doi:10.1109/I2MTC.2018.8409579.

- Baca, T., Petrlik, M., Vrba, M., Spurny, V., Penicka, R., Hert, D., Saska, M., 2021. The MRS UAV System: Pushing the Frontiers of Reproducible Research, Real-world Deployment, and Education with Autonomous Unmanned Aerial Vehicles. *Journal of Intelligent & Robotic Systems* 102, 1–28. doi:10.1007/s10846-021-01383-5.
- Bingham, B., Aguero, C., McCarrin, M., Klamo, J., Malia, J., Allen, K., Lum, T., Rawson, M., Waqar, R., 2019. Toward maritime robotic simulation in Gazebo, in: *Proceedings of MTS/IEEE OCEANS Conference*, Seattle, WA.
- Ccolque-Churquipa, A., Cutipa-Luque, J.C., Aco-Cardenas, D.Y., 2018. Implementation of a measurement system for the attitude, heading and position of a USV using IMUs and GPS, in: *2018 IEEE ANDESCON*, pp. 1–6. doi:10.1109/ANDESCON.2018.8564668.
- Deep, A., Mittal, M., Mittal, V., 2018. Application of Kalman filter in GPS position estimation, in: *2018 IEEE 8th Power India International Conference (PIICON)*, pp. 1–5. doi:10.1109/POWERI.2018.8704368.
- Diebel, J., 2006. Representing attitude: Euler angles, unit quaternions, and rotation vectors. *Matrix* 58, 1–35.
- Djapic, V., Prijic, C., Bogart, F., 2015. Autonomous takeoff & landing of small UAS from the USV, in: *OCEANS 2015 - MTS/IEEE Washington*, pp. 1–8. doi:10.23919/OCEANS.2015.7404595.
- Drawil, N.M., Amar, H.M., Basir, O.A., 2013. GPS localization accuracy classification: A context-based approach. *IEEE Transactions on Intelligent Transportation Systems* 14, 262–273. doi:10.1109/TITS.2012.2213815.
- Evangelidis, A., Parker, D., 2021. Quantitative verification of Kalman filters. *Formal Aspects of Computing* 33, 669–693. doi:10.1007/s00165-020-00529-w.
- Fossen, T.I., 1994. *Guidance and control of ocean vehicles*. Wiley.
- Fossen, T.I., 2002. *Marine Control Systems Guidance, Navigation, and Control of Ships, Rigs and Underwater Vehicles*. 1st edition ed., Marine Cybernetics, Trondheim.
- Fossen, T.I., 2011. *Handbook of Marine Craft Hydrodynamics and Motion Control*. First edition ed., John Wiley & Sons, United Kingdom.
- Fossen, T.I., Perez, T., 2009. Kalman filtering for positioning and heading control of ships and offshore rigs. *IEEE Control Systems Magazine* 29, 32–46. doi:10.1109/MCS.2009.934408.
- Gonzalez-Garcia, A., Miranda-Moya, A., Castañeda, H., 2021. Robust visual tracking control based on adaptive sliding mode strategy: Quadrotor uav - catamaran usv heterogeneous system, in: *2021 International Conference on Unmanned Aircraft Systems (ICUAS)*, pp. 666–672. doi:10.1109/ICUAS51884.2021.9476707.
- Grlj, C.G., Krznar, N., Pranjic, M., 2022. A decade of UAV docking stations: A brief overview of mobile and fixed landing platforms. *Drones* 6. doi:10.3390/drones6010017.
- Gupta, P.M., Pairet, E., Nascimento, T., Saska, M., 2023. Landing a uav in harsh winds and turbulent open waters. *IEEE Robotics and Automation Letters* 8, 744–751. doi:10.1109/LRA.2022.3231831.
- Han, Y., Ma, W., 2021. Automatic monitoring of water pollution based on the combination of UAV and USV, in: *2021 IEEE 4th International Conference on Electronic Information and Communication Technology (ICEICT)*, pp. 420–424. doi:10.1109/ICEICT53123.2021.9531204.
- Haykin, S., 2001. *Kalman Filtering and Neural Networks*. John Wiley & Sons, Inc, New York, USA. doi:10.1002/0471221546.
- Hert, D., Baca, T., Petracek, P., Kratky, V., Penicka, R., Spurny, V., Petrlik, M., Vrba, M., Zaitlik, D., Stoudek, P., Walter, V., Stepan, P., Horyna, J., Pritzl, V., Sramek, M., Ahmad, A., Silano, G., Bonilla Licea, D., Stibinger, P., Nascimento, T., Saska, M., 2023. MRS Drone: A Modular Platform for Real-World Deployment of Aerial Multi-Robot Systems. *Journal of Intelligent & Robotic Systems*.
- Hert, D., Baca, T., Petracek, P., Kratky, V., Spurny, V., Petrlik, M., Vrba, M., Zaitlik, D., Stoudek, P., Walter, V., Stepan, P., Horyna, J., Pritzl, V., Silano, G., Bonilla Licea, D., Stibinger, P., Penicka, R., Nascimento, T., Saska, M., 2022. MRS Modular UAV Hardware Platforms for Supporting Research in Real-World Outdoor and Indoor Environments, in: *2022 International Conference on Unmanned Aircraft Systems (ICUAS)*, IEEE. pp. 1264–1273. doi:10.1109/ICUAS54217.2022.9836083.
- Julier, S.J., Uhlmann, J.K., 1997. New extension of the Kalman filter to nonlinear systems, in: *Signal Processing, Sensor Fusion, and Target Recognition VI, International Society for Optics and Photonics*. SPIE. pp. 182–193. doi:10.1117/12.280797.
- Kalman, R.E., 1960. A new approach to linear filtering and prediction problems. *Journal of Basic Engineering* 82, 35–45. doi:10.1115/1.3662552.
- Kaur, H., Sahambi, J.S., 2016. Vehicle tracking in video using fractional feedback Kalman filter. *IEEE Transactions on Computational Imaging* 2, 550–561. doi:10.1109/TCI.2016.2600480.
- Krogus, M., Haggenmiller, A., Olson, E., 2019. Flexible layouts for fiducial tags, in: *IEEE/RSJ International Conference on Intelligent Robots and Systems (IROS)*.
- Kwak, J., Sung, Y., 2018. Autonomous UAV flight control for GPS-based navigation. *IEEE Access* 6, 37947–37955. doi:10.1109/ACCESS.2018.2854712.
- Lewandowski, W., Azoubib, J., Klepczynski, W., 1999. GPS: primary tool for time transfer. *Proceedings of the IEEE* 87, 163–172. doi:10.1109/5.736348.
- Li, W., Ge, Y., Guan, Z., Gao, H., Feng, H., 2023. Nmpc-based uav-usv cooperative tracking and landing. *Journal of the Franklin Institute* 360, 7481–7500. doi:10.1016/j.jfranklin.2023.06.023.
- Liu, W., Liu, Y., Bucknall, R., 2019. A robust localization method for unmanned surface vehicle (USV) navigation using fuzzy adaptive kalman filtering. *IEEE Access* 7, 46071–46083. doi:10.1109/ACCESS.2019.2909151.
- Lopez, A.R., 2010. GPS landing system reference antenna. *IEEE Antennas and Propagation Magazine* 52, 104–113. doi:10.1109/MAP.2010.5466404.
- Malyuta, D., Brommer, C., Hentzen, D., Stastny, T., Siegart, R., Brockers, R., 2020. Long-duration fully autonomous operation of rotorcraft unmanned aerial systems for remote-sensing data acquisition. *Journal of Field Robotics* 37, 137–157. doi:10.1002/rob.21898.
- Murphy, R., Stover, S., Pratt, K., Griffin, C., 2006. Cooperative damage inspection with unmanned surface vehicle and micro unmanned aerial vehicle at Hurricane Wilma, in: *2006 IEEE/RSJ International Conference on Intelligent Robots and Systems*, pp. 9–9. doi:10.1109/IROS.2006.282304.
- Murphy, R.R., Steimle, E., Griffin, C., Cullins, C., Hall, M., Pratt, K., 2008. Cooperative use of unmanned sea surface and micro aerial vehicles at Hurricane Wilma. *Journal of Field Robotics* 25, 164–180. doi:10.1002/rob.20235.
- Naab, C., Zheng, Z., 2022. Application of the unscented kalman filter in position estimation a case study on a robot for precise positioning. *Robotics and Autonomous Systems* 147, 103904. doi:10.1016/j.robot.2021.103904.
- Novak, F., Walter, V., Petracek, P., Baca, T., Saska, M., 2021. Fast collective evasion in self-localized swarms of unmanned aerial vehicles. *Bioinspiration & Biomimetics* 16, 066025. doi:10.1088/1748-3190/ac3060.
- Oh, S.R., Pathak, K., Agrawal, S., Pota, H., Garratt, M., 2006. Approaches for a tether-guided landing of an autonomous helicopter. *IEEE Transactions on Robotics* 22, 536–544. doi:10.1109/TRO.2006.870657.
- Olson, E., 2011. AprilTag: A robust and flexible visual fiducial system, in: *IEEE International Conference on Robotics and Automation (ICRA)*, IEEE. pp. 3400–3407.
- Petracek, P., Walter, V., Baca, T., Saska, M., 2020. Bio-inspired compact swarms of unmanned aerial vehicles without communication and external localization. *Bioinspiration & Biomimetics* 16, 026009. doi:10.1088/1748-3190/abc6b3.
- Polvara, R., Sharma, S., Wan, J., Manning, A., Sutton, R., 2018. Vision-based autonomous landing of a quadrotor on the perturbed deck of an unmanned surface vehicle. *Drones* 2. doi:10.3390/drones2020015.
- Ramirez, F.F., Benitez, D.S., Portas, E.B., Orozco, J.A.L., 2011. Coordinated sea rescue system based on unmanned air vehicles and surface vessels, in: *OCEANS 2011 IEEE - Spain*, pp. 1–10. doi:10.1109/Oceans-Spain.2011.6003509.
- Reidr, I., . Estimation II. Accessed: March 14, 2022. URL: <https://www.robots.ox.ac.uk/~ian/Teaching/Estimation/LectureNotes2.pdf>.

- Ribeiro, M.I., 2004. Kalman and extended kalman filters: Concept, derivation and properties. Institute for Systems and Robotics 43, 46.
- Santos, M.C., Bartlett, B., Schneider, V.E., Bradaigh, F.O., Blanck, B., Santos, P.C., Trslic, P., Riordan, J., Dooly, G., 2024. Cooperative unmanned aerial and surface vehicles for extended coverage in maritime environments. *IEEE Access* 12, 9206–9219. doi:10.1109/ACCESS.2024.3353046.
- Shao, G., Ma, Y., Malekian, R., Yan, X., Li, Z., 2019. A novel cooperative platform design for coupled USV–UAV systems. *IEEE Transactions on Industrial Informatics* 15, 4913–4922. doi:10.1109/TII.2019.2912024.
- Steenken, D., Winter, T., Zimmermann, U.T., 2001. Stowage and Transport Optimization in Ship Planning. Springer Berlin Heidelberg. pp. 731–745. doi:10.1007/978-3-662-04331-8_35.
- Tomera, M., 2012. Nonlinear observers design for multivariable ship motion control. *Polish Maritime Research* , 50–56.
- Tran, Q.V., Ahn, H.S., 2019. Multi-agent localization of a common reference coordinate frame: An extrinsic approach. *IFAC-PapersOnLine* 52, 67–72. doi:10.1016/j.ifacol.2019.12.128. 8th IFAC Workshop on Distributed Estimation and Control in Networked Systems NECSYS 2019.
- Walter, V., N.Staub, Saska, M., Franchi, A., 2018a. Mutual localization of UAVs based on blinking ultraviolet markers and 3D time-position Hough transform, in: 14th IEEE International Conference on Automation Science and Engineering (CASE 2018).
- Walter, V., Saska, M., Franchi, A., 2018b. Fast mutual relative localization of UAVs using ultraviolet LED markers, in: 2018 International Conference on Unmanned Aircraft System (ICUAS 2018).
- Walter, V., Staub, N., Franchi, A., Saska, M., 2019. UVDAR system for visual relative localization with application to leader–follower formations of multirotor UAVs. *IEEE Robotics and Automation Letters* 4, 2637–2644. doi:10.1109/LRA.2019.2901683.
- Walter, V., Vrba, M., Saska, M., 2020. On training datasets for machine learning-based visual relative localization of micro-scale UAVs, in: 2020 IEEE International Conference on Robotics and Automation (ICRA), pp. 10674–10680.
- Wang, J., Olson, E., 2016. AprilTag 2: Efficient and robust fiducial detection, in: IEEE/RSJ International Conference on Intelligent Robots and Systems (IROS).
- Wang, N., Zhu, Z., Qin, H., Deng, Z., Sun, Y., 2021a. Finite-time extended state observer-based exact tracking control of an unmanned surface vehicle. *International Journal of Robust and Nonlinear Control* 31, 1704–1719. doi:10.1002/rnc.5369.
- Wang, Y., He, X., Liu, D., Qin, J., Li, P., 2021b. States estimation for unmanned surface vehicles (USVs) using Dual Unscented Kalman filters, in: 2021 International Conference on Intelligent Computing, Automation and Applications (ICAA), pp. 911–916. doi:10.1109/ICAA53760.2021.00166.
- Wendel, J., Meister, O., Schlaile, C., Trommer, G.F., 2006. An integrated GPS/MEMS-IMU navigation system for an autonomous helicopter. *Aerospace Science and Technology* 10, 527–533. doi:10.1016/j.ast.2006.04.002.
- Wirtensohn, S., Schuster, M., Reuter, J., 2016. Disturbance estimation and wave filtering using an Unscented Kalman filter. *IFAC-PapersOnLine* 49, 518–523. doi:10.1016/j.ifacol.2016.10.488. 10th IFAC Conference on Control Applications in Marine SystemsCAMS 2016.
- Xiao, X., Dufek, J., Woodbury, T., Murphy, R., 2017. UAV assisted USV visual navigation for marine mass casualty incident response, in: 2017 IEEE/RSJ International Conference on Intelligent Robots and Systems (IROS), pp. 6105–6110. doi:10.1109/IROS.2017.8206510.
- Xu, Z.C., Hu, B.B., Liu, B., Wang, X., Zhang, H.T., 2020a. Vision-based autonomous landing of unmanned aerial vehicle on a motional unmanned surface vessel, in: 2020 39th Chinese Control Conference (CCC), pp. 6845–6850. doi:10.23919/CCC50068.2020.9188979.
- Xu, Z.C., Hu, B.B., Liu, B., Wang, X., Zhang, H.T., 2020b. Vision-based autonomous landing of unmanned aerial vehicle on a motional unmanned surface vessel, in: 2020 39th Chinese Control Conference (CCC), pp. 6845–6850. doi:10.23919/CCC50068.2020.9188979.
- Young, S., Peschel, J., Penny, G., Thompson, S., Srinivasan, V., 2017. Robot-assisted measurement for hydrologic understanding in data sparse regions. *Water* 9. doi:10.3390/w9070494.